



저작자표시-비영리-변경금지 2.0 대한민국

이용자는 아래의 조건을 따르는 경우에 한하여 자유롭게

- 이 저작물을 복제, 배포, 전송, 전시, 공연 및 방송할 수 있습니다.

다음과 같은 조건을 따라야 합니다:



저작자표시. 귀하는 원저작자를 표시하여야 합니다.



비영리. 귀하는 이 저작물을 영리 목적으로 이용할 수 없습니다.



변경금지. 귀하는 이 저작물을 개작, 변형 또는 가공할 수 없습니다.

- 귀하는, 이 저작물의 재이용이나 배포의 경우, 이 저작물에 적용된 이용허락조건을 명확하게 나타내어야 합니다.
- 저작권자로부터 별도의 허가를 받으면 이러한 조건들은 적용되지 않습니다.

저작권법에 따른 이용자의 권리는 위의 내용에 의하여 영향을 받지 않습니다.

이것은 [이용허락규약\(Legal Code\)](#)을 이해하기 쉽게 요약한 것입니다.

[Disclaimer](#)

Deep Learning Enhanced Individual Nuclear-Spin Detection in Complex Electron-Nuclear Spin Systems

A Thesis Presented

by

Kyunghoon Jung

A Thesis Submitted to the Faculty of Seoul National University
In Partial Fulfillment of the Requirement for
the Degree of Master of Physics

June 2020

Department of Physics and Astronomy
The Graduate School
Seoul National University

© Copyright by Kyunghoon Jung 2020

All Rights Reserved

ABSTRACT

This thesis presents a novel methodology for specifying individual nuclear spins which interact with a nitrogen-vacancy (NV) defect center in diamond. One of numerous point defects in diamond, the NV center, is an optically active color center consisting of one substitutional nitrogen atom and an adjacent vacancy in the diamond lattice. A spin state of an electron in the NV center changes depending on hyperfine interaction with nuclear spins of ^{13}C isotopes.

In this work, we develop a deep neural network-based algorithm that can efficiently and automatically analyze nuclear spins coupled to a single electron spin. We focus on CPMG-type dynamical decoupling spectroscopy, which is widely employed for single nuclear spin detection and control and is a common starting point for more advanced spectroscopy methods. We demonstrate that our deep learning approach enables fast automatic nuclear spin detection by decomposing sophisticated spectral data that has been difficult to be analyzed so far. These results enable efficient imaging of complex spin samples and automatic characterization of large spin-qubit registers.

Keywords: NV center, CPMG(The Carr-Purcell-Meiboom-Gill) signal, deep learning, hyperfine interaction

Student Number: 2010-20380

TABLE OF CONTENTS

	Page
ABSTRACT	ii
LIST OF TABLES	iv
LIST OF FIGURES	v
CHAPTER 1. Introduction	1
1.1 The quantum computing	1
1.2 The nitrogen-vacancy center in diamond.....	1
1.3 State Structure of NV center.....	3
CHAPTER 2 Dynamical Decoupling Pulse Sequence.....	5
2.1 Hahn echo (spin echo) and CPMG (Carr-Purcell-Meiboom-Gill) pulse	5
2.2 Recent advances and proposed methodology.....	10
CHAPTER 3 Deep Learning Models for analyzing CPMG signal.	14
3.1 Data Representation	15
3.2 Fully connected based model for period classification.....	17
3.3 1D-Convolutional based model for noise recovery.....	19
3.4 Fully connected based model for regression and fine-tuning step	22
3.5 Comparison with previous experimental results	22
CHAPTER 4 Discussion.....	25
CHAPTER 5 Supplementary Information.....	27
BIBLIOGRAPHY	55
ACKNOWLEDGMENT	61
Abstract in Korean (국문 초록)	62

LIST OF TABLES

Table	Page
1.1. Table S1. Rearranged DFT lists according to the target periods used for HPC models	36
1.1. Table S2. The resulting hyperfine parameters (A , B) and corresponding confidence scores of the HPC models	40

LIST OF FIGURES

Figure	Page
Figure 1. The nitrogen-vacancy (NV) center in diamond.....	2
Figure 2. The energy level of NV center at room temperature	3
Figure 3. Pulse diagram of spin echo and CPMG n-pulse sequence.	5
Figure 4. Simulated CPMG signals for a single and double ¹³ C nuclear spin	7
Figure 5. Simulated CPMG signals for multiple ¹³ C nuclear spins	9
Figure 6. General procedure for identifying hyperfine parameters of ¹³ C nuclear spins	12
Figure 7. Individual spin signature identification by hyperfine parameter classifier (HPC) deep learning model.....	14
Figure 8. Denoising and decoherence effect recovery procedure	19
Figure 9. Multiple nuclear spin detection from experimental data.....	21
Figure S1. Range of hyperfine parameters (A, B) used for proposed models	27
Figure S2. Flow chart of the deep learning protocol and experimental CPMG measurement	28
Figure S3. Histogram of the Gaussian distribution used for generating noisy training datasets	29
Figure S4. Experimental sequence.....	30
Figure S5. Results from HPC models.....	31
Figure S6. Identifying a group of spins for a single broad dip.....	32
Figure S7. Receiver operating characteristic (ROC) curves and corresponding confusion matrices for HPC models	33
Figure S8. Verification of nuclear spin detection in N=96 and N=128.....	34
Figure S9. Comparison of CPMG signals with or without nuclear-nuclear interaction...	35

Chapter 1. Introduction

1.1 The quantum computing

The quantum computer has been highlighted for many years and has still remained a challengeable field. One of the elementary building blocks being named a qubit (quantum bit) can exist in an arbitrary superposition state of 0 and 1, which is a core characteristic to enable quantum supremacy [1].

One of challenges relates to an effect on this quantum state, which is called decoherence. Quantum decoherence, the irreversible loss of quantum information, results from unintended interactions with the environment. In this context, a magnetic moment of a single impurity atom, such as an electron in the nitrogen-vacancy center in diamond, is an admirable candidate because it shows a relatively long coherence time and its scalability [2, 3].

1.2 The nitrogen-vacancy center in diamond

The nitrogen-vacancy (NV) center in diamond consisting of a single impurity atom with coupled electrons has had much attention especially due to its characteristic of being coherently manipulated with high fidelity even at room temperature and also it is relatively easy to initialize and read out the electron spin [3]. In addition, the NV center has spin-dependent optical transitions which enables the quantum state to be transmitted over long distances via photons [2, 3].

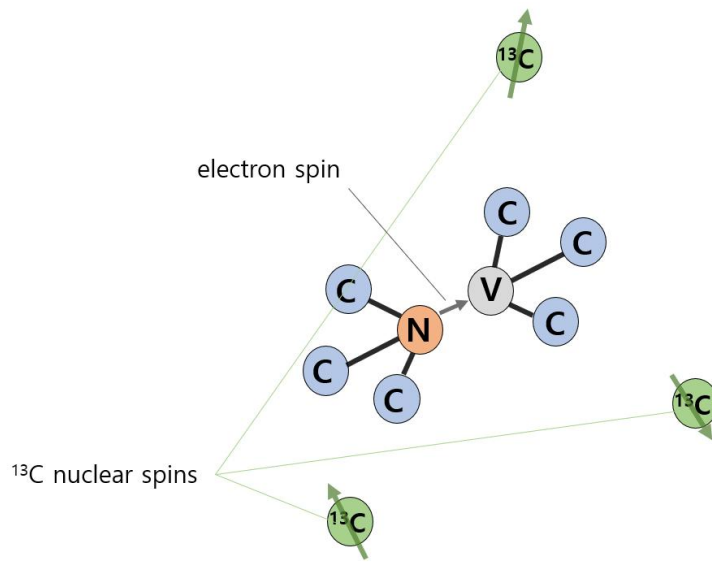


Figure 1. The nitrogen-vacancy center in diamond consisting of a nitrogen atom (N) with a vacant lattice site (V) and neighboring carbon atoms (C and ^{13}C).

In Fig.1, the electron spin is coupled with a nuclear spin of the nitrogen atom and nearby nuclear spins of ^{13}C atoms. The electron has a large gyromagnetic ratio and shows a relatively long coherence time so that the electron spin state is harnessed to identify coupling parameters of hyperfine interaction with ^{13}C nuclear spins.

1.3 State Structure of NV center

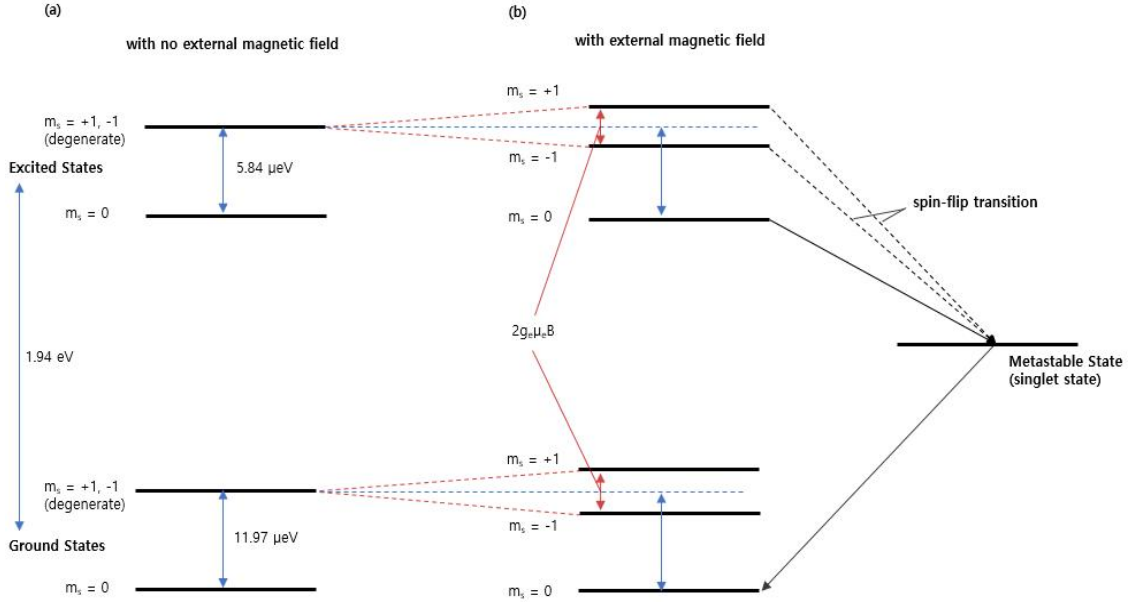


Figure 2. The energy level of NV center at room temperature. The energy level in (a) no external magnetic field and (b) an applied external magnetic field

Energy levels of the NV center are depicted in Fig.2. The energy level of NV center has attracted many attentions through theoretical and experimental studies so far [3]. There are five valence electrons in a nitrogen atom, where three of them covalently bond to the carbon atoms and two remain non-bonded named as a lone pair. Similarly, there are three unpaired electrons in the vacancy, where two of them make a quasi-covalent bond and one stays unpaired.

With an external magnetic field, spin triplet with $m_s = +1, -1$ are separated by $+g_e\mu_e B, -g_e\mu_e B$ respectively. There exists metastable state of a singlet spin state, also called as a shelving state, between ground states and excited states. The metastable state is essential to obtain intended spin states.

Through continuous optical excitations using a spin-dependent relaxation procedure, the electron spin state of NV center can be initialized into the $m_s=0$ state. During excitation processes, spin-flips mainly happen through decay via the metastable state. Decay from $m_s=+1, -1$ into the metastable state happens much more than from $m_s=0$ into the metastable state. On the other hand, decay from the metastable state into the ground state happens primarily into the $m_s=0$ state than into $m_s=+1$ or -1 . Therefore, the ground state of $m_s=0$ becomes occupied more and more as the optical excitation process continues.

Chapter 2. Dynamical Decoupling Pulse Sequence

2.1 Hahn echo (spin echo) and CPMG (Carr-Purcell-Meiboom-Gill) pulse sequence

2.2.1 Hahn echo

Reducing a decoherence effect is a crucial procedure in a state spectroscopy to extend more measurement time. The Hahn echo (or spin echo) sequence is introduced to decouple NV spins from the decoherence [3, 4]. This technique refocuses a spin magnetization by a pulse of resonant electromagnetic radiation.

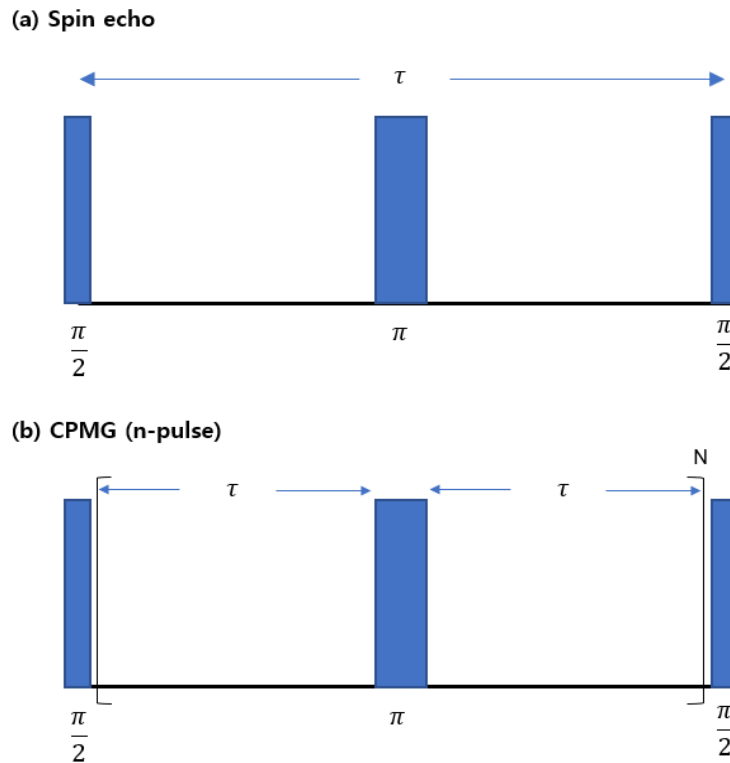


Figure 3. Pulse diagram of spin echo and CPMG n-pulse sequence.

The nuclear magnetic resonance (NMR) signal which is initialized into a specific state decays due to both spin relaxation and inhomogeneous effects which make each spin in diamond rotate at each different precession rate. While the spin relaxation leads to

an irreversible loss of magnetization, the inhomogeneous dephasing can be reduced by applying a 180° inversion (or π) pulse (Fig.3a) that inverts the magnetization vectors [4], where its technique is named as a spin echo.

2.2.2 CPMG

The spin echo technique only decouples NV spins from filed fluctuations that are slow compared to the free precession time. To decouple single NV spins from higher interacting frequencies, various dynamical decoupling techniques have been studied. Among them is the CPMG pulse sequence, widely used in the field of NMR [4], which is an extension of the spin echo sequence where the single refocusing π pulse is replaced with periodically spaced π pulses. In Fig.3 (b), the number of repetitions of π pulses is N.

2.2.3 Characteristics of the experimental CPMG signal

The probability of the electron spin state can be obtained by the equation (1) [5].

$$P_x = \frac{1 + \prod_{k=1}^n M_k}{2} \quad (1)$$

$$M_k = 1 - (1 - \hat{n}_0 \cdot \hat{n}_1) \sin^2 \frac{N\varphi}{2} \quad (2)$$

$$\varphi = \cos^{-1}(\cos \alpha \cos \beta - m_z \sin \alpha \sin \beta) \quad (3)$$

$$1 - \hat{n}_0 \cdot \hat{n}_1 = m_x^2 \frac{(1 - \cos \alpha)(1 - \cos \beta)}{1 + \cos \alpha \cos \beta - m_z \sin \alpha \sin \beta} \quad (4)$$

$$\text{where } m_z = \frac{A_k + \omega_L}{\tilde{\omega}}, m_x = \frac{B_k}{\tilde{\omega}}, \tilde{\omega} = \sqrt{(A_k + \omega_L)^2 + B_k^2}, \alpha = \tilde{\omega}t, \beta = \omega_L t$$

P_x is the probability of the electron spin state, φ is a rotation angle of the net evolution of the nuclear spin after a single decoupling unit, \hat{n}_i is an axis of a rotation angle (φ) which depends on the initial state of the electron spin; \hat{n}_0 corresponds to an initial state $m_s = 0$, \hat{n}_1 to initial states $m_s = +1, -1$, k is an index of k^{th} nuclear spin, n is the total number of nuclear spins, A (B) is the longitudinal (transverse) hyperfine interaction parameter and finally ω_L is the Larmor frequency of an interacting nuclear spin.

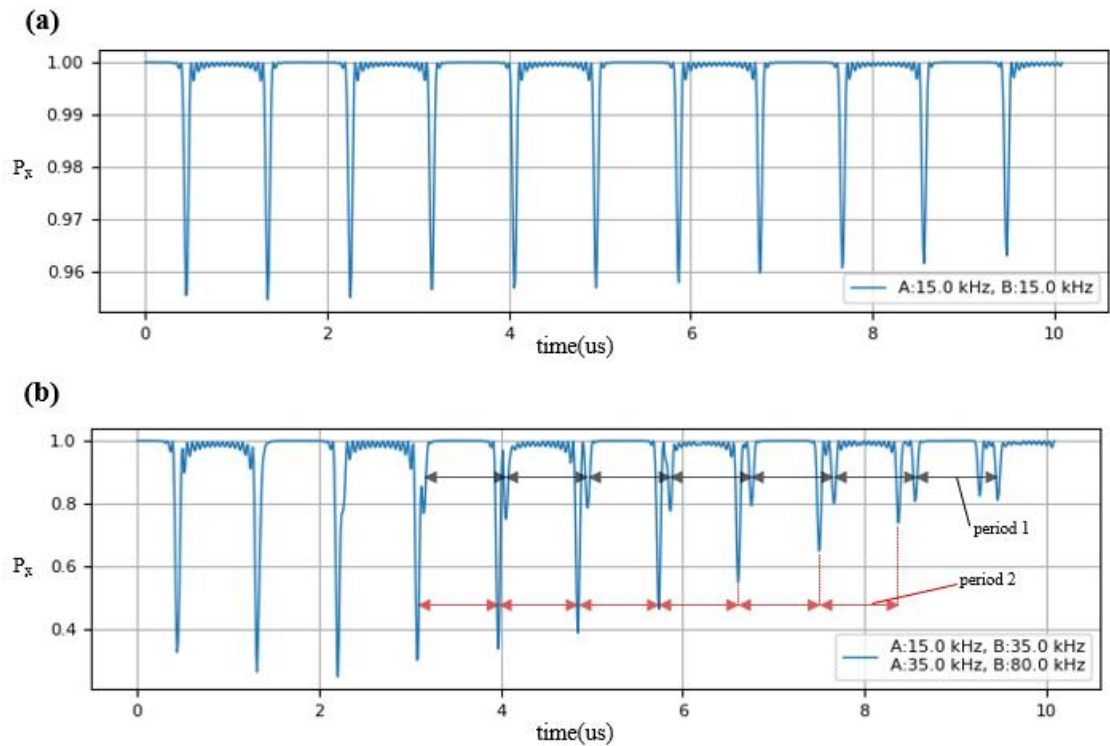


Figure 4. Simulated CPMG signals for a single and double nuclear spin ($N=8$) (a) A typical pattern of single interacting nuclear ^{13}C spin. The dips form with a specific period corresponding to the interacting nuclear spin. (b) two different periods relating with different nuclear spins.

If there are one or two interacting ^{13}C nuclear spins, it shows a typical periodicity of dips corresponding each nuclear spin. (Fig. 4 (a) corresponds to one nuclear spin, (b) to two nuclear spins) The period of dips directly relates to a pair of

hyperfine parameters (A , B) of a corresponding nuclear spin (see Eqns (1)-(4)). For example, in Fig 4 (b), period 1 correlates with a spin with A : 15 kHz, B :35 kHz and period 2 with A : 35 kHz, B : 80 kHz. Therefore, through analyzing periods of dips, hyperfine parameters of corresponding nuclear spins can be obtained.

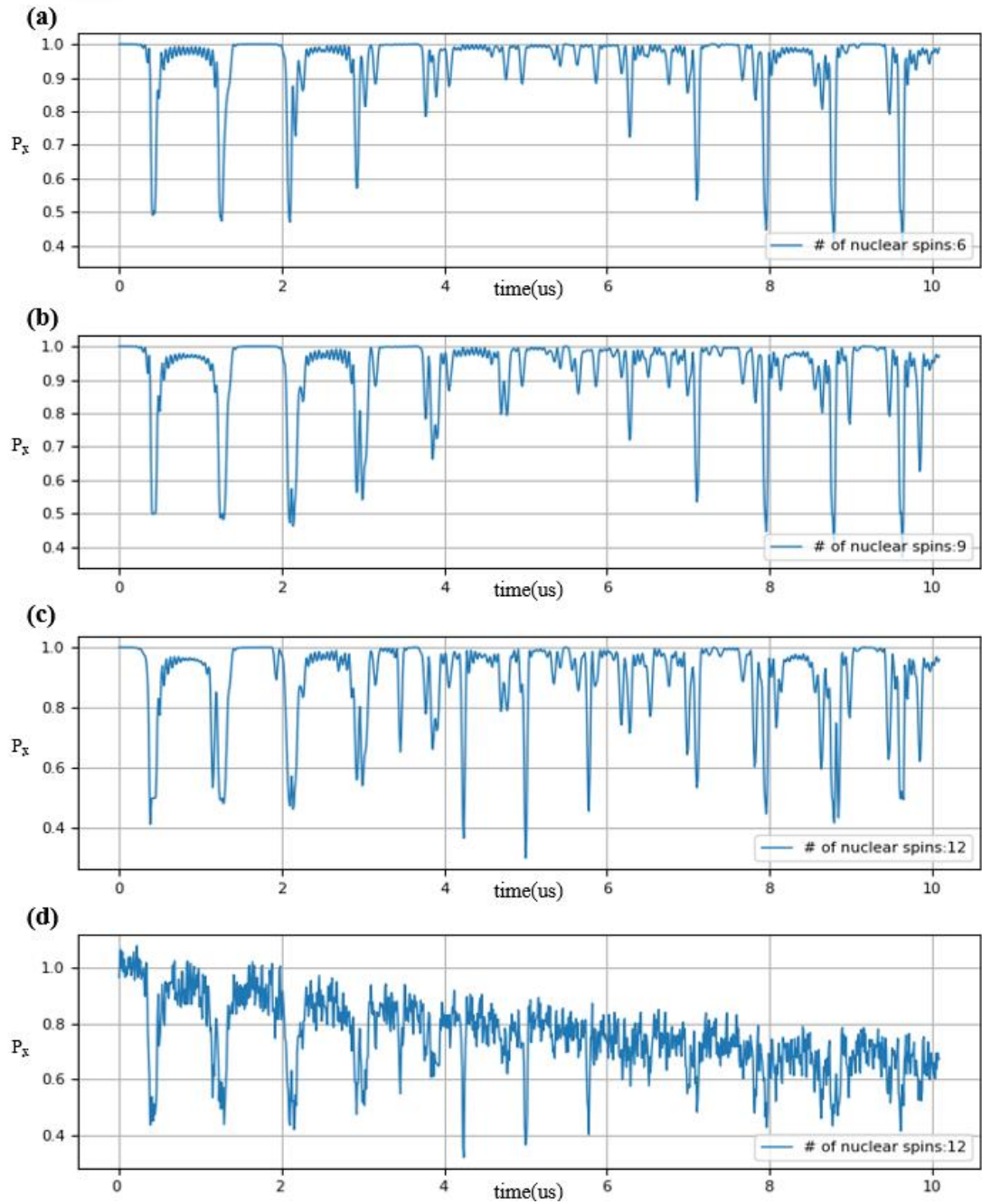


Figure 5. (a) ~ (c) Simulated CPMG signals for multiple ^{13}C nuclear spins. Each of them corresponds to the number of 6, 9, 12 nuclear spins, respectively. (d) CPMG signal with the same (A, B) coefficients of (c) added with a random noise and a decoherence effect.

But, if there exist several ^{13}C nuclear spins, such as 6 or 9 nuclear spins, the situation turns different. In Fig 5, it shows CPMG signals induced by a few different ^{13}C nuclear spins. In contrast to the case in Fig 4, it is difficult to figure out each period of dips. Because P_x is not just a linear sum of all the P_x values of each spin but each M value (see Eqn. (1) and (2)) of nuclear spins are multiplied with each other. (if there are k nuclear spins, $M_{\text{total}} = M_1 \cdot M_2 \cdot M_3 \cdot M_4 \cdot \dots \cdot M_k$) This makes difficult to analyze the CPMG signals in a case of many ^{13}C nuclear spins.

In Fig. 5 (d), it shows CPMG signals with a simulated noise and decoherence effect. A noise makes small dips indistinguishable if a dip is compatible to an amplitude of noises and a decoherence effect makes the signal decays. So, overall shape is sophisticated to capture distinct features and related hyperfine parameters of nuclear spins. This characteristic introduces an additional complexity compared to conventional nuclear magnetic resonance (NMR) signals [6-8] and, along with the decoherence and environmental noises, makes existing NMR peak decomposition packages [9-14] ineffective for analyzing the signal.

2.2 Recent advances and proposed methodology.

Recent studies in the control of single electron spins associated to defects in solids have enabled the sensing, imaging and control of individual nuclear spins [15-29]. From a quantum sensing perspective, this has enabled the detection and imaging of nuclear spins with atomic-scale resolution and single spin sensitivity, in systems of up to 27 spins [19, 24, 30-33]. From a quantum information perspective, controlling individual nuclear spins provides quantum registers for quantum computation and optically-connected quantum networks [34-37]. Proof-of-principle experiments have demonstrated

quantum registers with 10+ qubits [28, 34-38], elementary quantum algorithms and error correction protocols [19, 39-44] and key quantum network protocols such as entanglement distillation [45, 46].

An important task in both these application fields is to detect and identify the nuclear spins, and to characterize the electron-nuclear interaction. For imaging larger, more complex, spin structures and for the realization of large-scale quantum networks that consist of many multi-qubit devices, it is required to develop objective and automated methods that can efficiently identify signatures of nuclear spins and determine coupling parameters from experimental spectroscopy.

In this work, we develop neural-network-based algorithms that can efficiently and automatically detect nuclear spins by their coupling to a single electron spin. We focus on CPMG-type dynamical decoupling spectroscopy [5, 35, 47, 48], which is widely employed for single nuclear spin detection and control [5, 49] and is a common starting point for more advanced spectroscopy methods [23, 24, 27, 32]. While our methods are general, we exemplify them through experiments on a single nitrogen-vacancy (NV) center in diamond with nearby naturally abundant ^{13}C nuclear spins [5, 19, 35]. We show that our deep learning approach enables fast automatic nuclear spin detection and hyperfine parameter estimation for 31 individual spins.

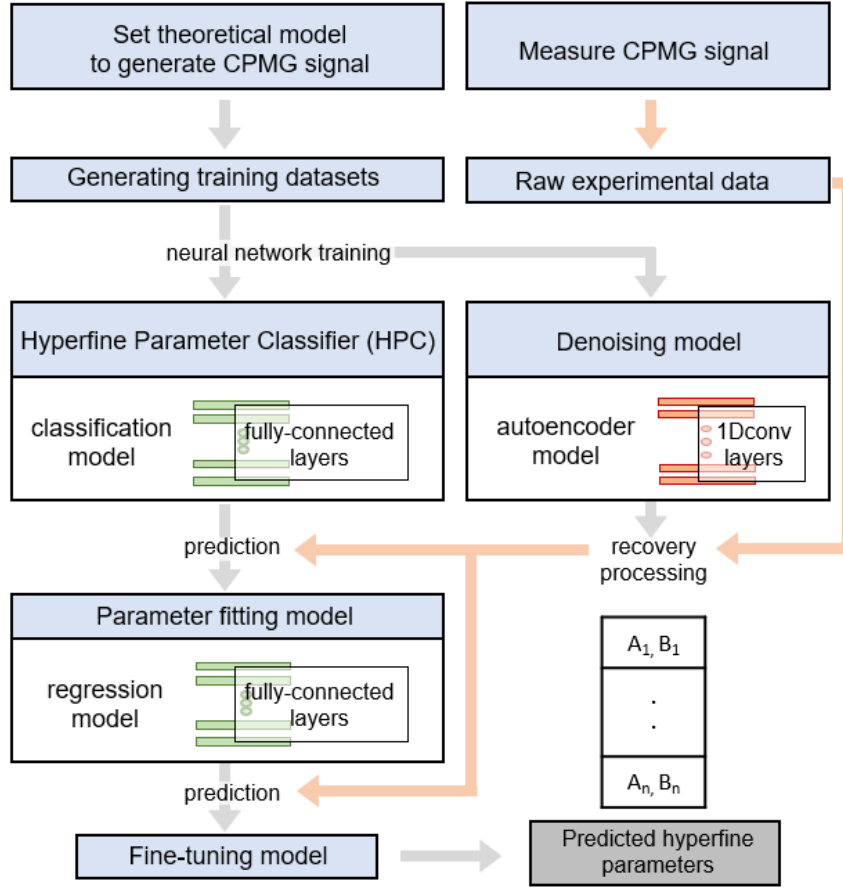


Figure 6. General procedure for identifying hyperfine parameters of ^{13}C nuclear spins. Pseudo-algorithm for training and hyperfine-parameters-prediction sequences including hyperfine parameter classifier (HPC), denoise and signal recovery, regression-based fitting, and fine-tuning models. The flow of experimental processes (computational processes) is on the red (gray) arrows.

The main task of our deep learning model is to efficiently encode the features of each k^{th} nuclear spin in Eqn. (1). Once successfully trained, the models can determine A_k and B_k of each nuclear spin from the experimental spectroscopy data. Figure 6 shows the overall procedure to achieve this task. First, the measurements of CPMG signals and the implementations for generating datasets and training deep learning models are conducted simultaneously. Generating datasets for both HPC models and denoising models is

performed using the theoretical model in Eqn. (1). Second, via the generated training datasets, denoising models are trained to reduce noise and HPC models are trained to identify whether specific hyperfine parameters exist in the data or not. Third, to enhance signal-to-noise ratio, the raw noisy CPMG signal is pre-processed by the trained denoising model and decoherence recovery process and is fed into the trained HPC models. Fourth, using the outputs of the HPC models, an additional deep learning-based regression model is adapted to further restrict possible hyperfine parameter combinations. Lastly, in the auto fine-tuning phase, the prediction of the regression model is used as initial values of the hyperfine parameters, and automatic numerical fitting is performed.

Chapter 3. Deep Learning Models for analyzing CPMG signal

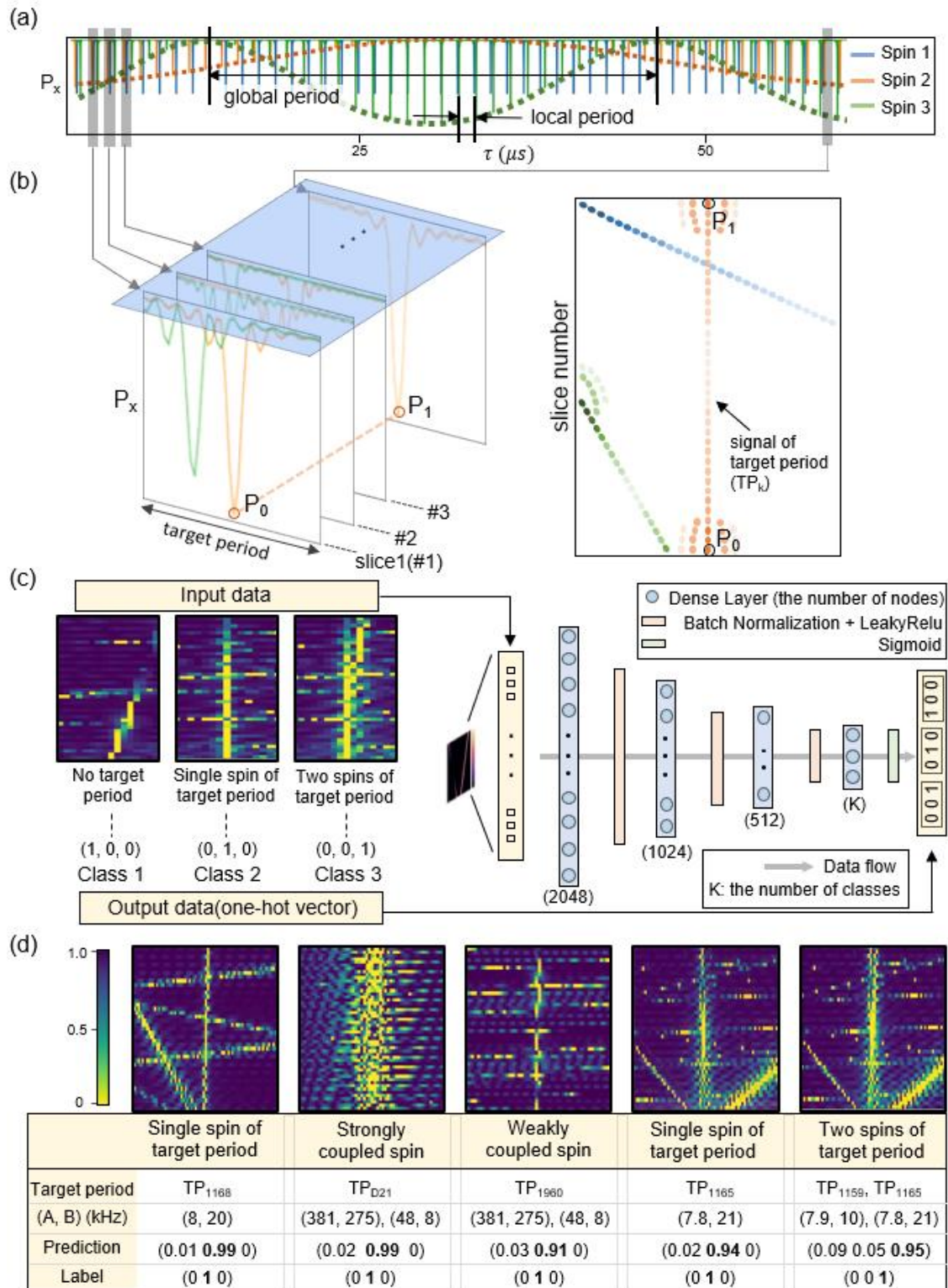


Figure. 7. Individual spin signature identification by hyperfine parameter classifier (HPC) deep learning model. (a) Simulated CPMG signal with three spins of different (A , B) values showing general features of nuclear spectra including local and global periods (see text for definitions). (b) Concept of the data conversion into 2D images by slicing and stacking the data fragments with specified target period TP_k . This reveals the signature of a target signal as a vertical line with vanishing slope, which is generally superposed with other interfering nuclear spin signals. (c) Training datasets and architecture of the HPC model in a case of classifying three classes ($K=3$), where K is the number of nodes of the last layer. The input data consists of three different classes, where each class corresponds to the number of existing nuclear spins with the target period, and the output data is one-hot vector form assigned to each class. For example, Class 1 (Class 2) means that no (one) spin with the target period exists. (d) Example predictions of the HPC model depending on hyperfine coupling strength (first to third panels) and proximity to similar period (fourth and fifth panels). For all cases, the HPC model predicts correct spin signatures corresponding to input signals showing good consistency between the predicted vectors and the output vectors. (for example, in the first panel, the predicted vector is (0.01 0.99 0) and the output vector is (0 1 0)). The color scale bar in all 2D images ranges from 0 to 1.

3.1 Data Representation

The qualitative features of a typical dynamical decoupling signal are as follows.

First, the coherence dip of k^{th} nuclear spin is periodic with approximate periodicity [5]

(local period)

$$TP_k = 2\pi / (\tilde{\omega}_k + \omega_L) \quad (4)$$

where $\tilde{\omega}_k = \sqrt{(A_k + \omega_L)^2 + B_k^2}$, and A_k and B_k are hyperfine parameters of the ' k^{th} target' local period (see Figure S1 for the range of A and B values used in the proposed model).

Second, the envelop of the coherence dip amplitudes as a function of τ is periodic essentially showing periodic quantum entanglement evolution with the resonant nuclear spin (global period). Third, each coherence dip can show additional fringes depending on the hyperfine interaction strength. In the strong coupling regime, for example when $B > 100$ kHz, CPMG signal is shown to exhibit multiple and large fringe oscillations [5, 19] (Eqn. (2) and (3)). While conventional numerical peak detection or Fourier transform

analysis is inefficient in the presence of these oscillating signals, below we show that the deep learning approach offers an excellent alternative route to solve the problem.

In principle, supervised learning algorithms can be applied using the theoretical model given by Eqns. (1)-(3) for this nominally multi class classification problem [50-54]. The data preparation and training, however, is challenging in that, (1) the number of nuclear spins interacting with central NV center is not known *a priori* and (2) the number of possible (A, B) pair combinations for a given number of surrounding nuclear spins is large. Brute force generation of large datasets with variable number of nuclear spins is impractical and generally not reliable to represent possible spin configurations unambiguously.

We convert the multi class classification problem to that of single class by reorganizing the data so that the deep learning model focuses on identifying a single target spin. Figure 7 (b) shows the general concept of this conversion. By cutting the CPMG signal according to the TP_k of a target spin and making a 2D image by stacking multiple slices, the difference of the local periods between two spins can be distinguished. The features of the global period can be also analyzed by the distribution of pixel values on the vertical axis. With this representation, the deep learning model analyzes whether the target spin signal marked by a vertical line exists in the 2D image. Moreover, non-linear oscillations near the main coherence dip in the strong coupling regime, which are difficult to address by hand-crafted coding, generally appear as fringe patterns in this data representation. The deep learning model shows a strong ability of

classifying target signals in the presence of these interfering patterns through image recognition [55, 56].

3.2 Fully connected based model for period classification

Focusing on the local period of a specific target spin signal, we develop a set of deep learning models, coined HPC, each of which classifies the existence of a specific period of hyperfine-induced coherence dips in the data. Figure 7 (c) illustrates a structure of the HPC model and training datasets by exemplifying a case of classifying three different classes (see a detailed implementation of generating training datasets in Note S2). The input training data is prepared along with three output classes as shown in Fig. 7 (c). Class 1 corresponds to data that does not contain a spin with the target period, class 2 is for one spin with the target period existing in the data, and class 3 for two spins with slightly dissimilar target periods in the data. The output data is denoted in *one-hot vector* form; $(1, 0, 0)$, $(0, 1, 0)$, and $(0, 0, 1)$ corresponding to no, single, and double target periods, respectively. The model is trained to estimate the confidence score of each element of the three-dimensional vector according to the input image. The model consists of stacked layers of Dense layer, Batch Normalization layer [57] and LeakyRelu activation function as shown in Fig. 7 (c). The detailed procedure of the neural network development is described in the methods section and Figure S2 and Note S2.

Panels in Fig. 7 (d) show the classification results using our HPC model. The first panel is for the typical case that a single target period exists without strong disturbance from other spins nor spin bath signal, and the model successfully outputs a vector close to $(0, 1, 0)$. The second panel shows the performance of the model for a

strongly coupled single target spin where the parameters for spin number TP_{D21} in Table S1, taken from existing density functional theory (DFT) calculations [58], is used as an example. As mentioned above, although the spin signal is superposed with wide fringe patterns and oscillations, the model successfully identifies the signature of the target period with the output vector reaching (0.002, 0.99, 0). The third panel shows that the model also successfully classifies the target period even in the presence of other superposed strongly coupled spin signals. Furthermore, the fourth and the fifth panels give an example of the performance for input datasets with a single spin, $(A_2, B_2)/2\pi = (7.8, 20)$ (kHz) (fourth panel) and with two spins of similar local period, $(A_1, B_1)/2\pi = (7.9, 10)$, $(A_2, B_2)/2\pi = (7.8, 20)$ (kHz), (fifth panel). The model successfully distinguishes each case, showing high selectivity of the nuclear spins. Therefore, these results show that our deep learning model provides a promising approach to detect individual nuclear spins with high precision, high selectivity, and for a wide range of hyperfine strengths.

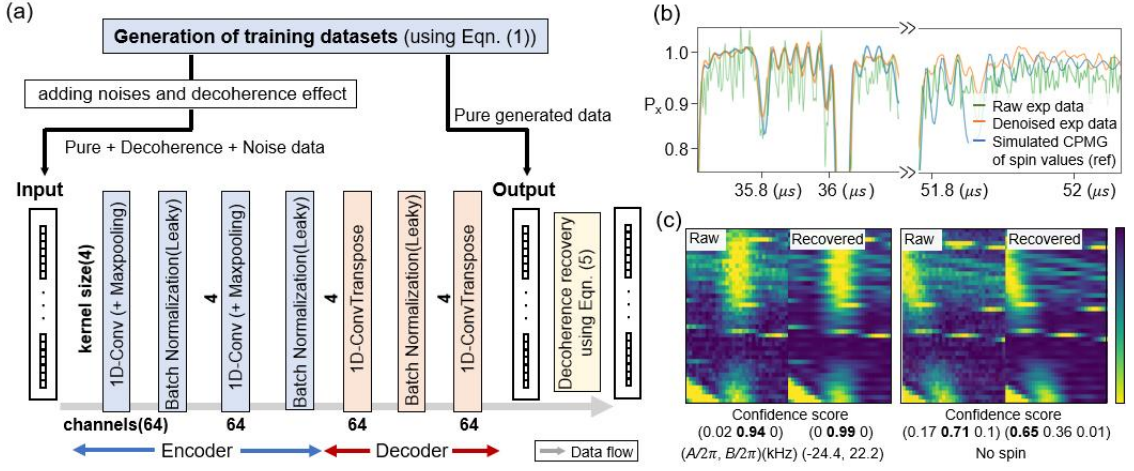


Figure 8. Denoising and decoherence effect recovery procedure. (a) Architecture of the signal recovery model. The pure data is generated by Eqn. (1). The noisy data is generated with adding decoherence effects and noise to the pure data using Eqn. (5). The model is trained to reproduce denoised data from the noisy data and the decoherence effect is recovered using Eqn. (5). (b) Raw experimental (green), pure (blue), and recovered (orange) CPMG data showing successful recovery of the fringe patterns in the presence of noise with a comparable amplitude. The figure also shows signal recovery performance in the long evolution time regime. (c) The comparison of the raw experimental data with the noise recovered data in the 2D image form used for HPC model analysis showing an enhancement in signal-to-noise ratio and predictability. The color scale bar in all 2D images ranges from 0 to 1.

3.3 1D-Convolutional based model for noise recovery

Before evaluating the experimental CPMG signal by trained HPC models, we first pre-process the raw experimental data by a denoising model. Figure 8 (a) shows the overall procedure. For the noise removal process, Gaussian noise with the standard deviation $\sigma = 0.05$ reflecting the experimental noise is added to the training datasets (see Figure S3). The decoherence effect is modelled by the approximate equation [5],

$$P_x = \frac{1}{2} M \cdot \exp\left(-\frac{\tau}{T}\right)^n + \frac{1}{2} \quad (5)$$

, where T accounts for dephasing of the electron spin, n is an exponential power obtained by fitting the experimental data and τ is half of the inter-pulse delay. We use an

autoencoder structure [59, 60], which is an established structure to learn the representations of input data, to encode the features of the noisy input data and generate the denoised data. A one-dimensional convolution (1D CNN) layer [61], which is widely used to capture the features of one-dimensional data such as time-series signal, is employed for building the denoising neural network.

As shown in Fig. 8 (b), the signal recovery model effectively removes the noises while retaining nuclear spin signatures of the experimental data. This is highlighted with the capability of recovering detailed oscillatory features of the data where the amplitudes of signals are almost equivalent to the fluctuations due to noise. Panels in Fig. 8 (c) compares the visibility of the spin signal of the raw (left panel) and the processed (right panel) data showing effective removal of experimental noise and enhancement of signal-to-noise ratio, leading to higher performance of prediction by the HPC model. After denoising the raw experimental data, the decoherence effect is recovered by applying Eqn. (5) to the denoised data. We find that the confidence scores from HPC evaluating denoised experimental data are, in general, a few percent higher than evaluating raw data (compare (0.02, 0.91, 0) vs. (0, 0.99, 0) in Fig. 8 (c) and in some cases false predictions of raw data are corrected in denoised data (compare (0.17 0.71 0.1) vs (0.65 0.36 0.01) in Fig. 8 (c), successfully showing the efficiency of our pre-processing model.

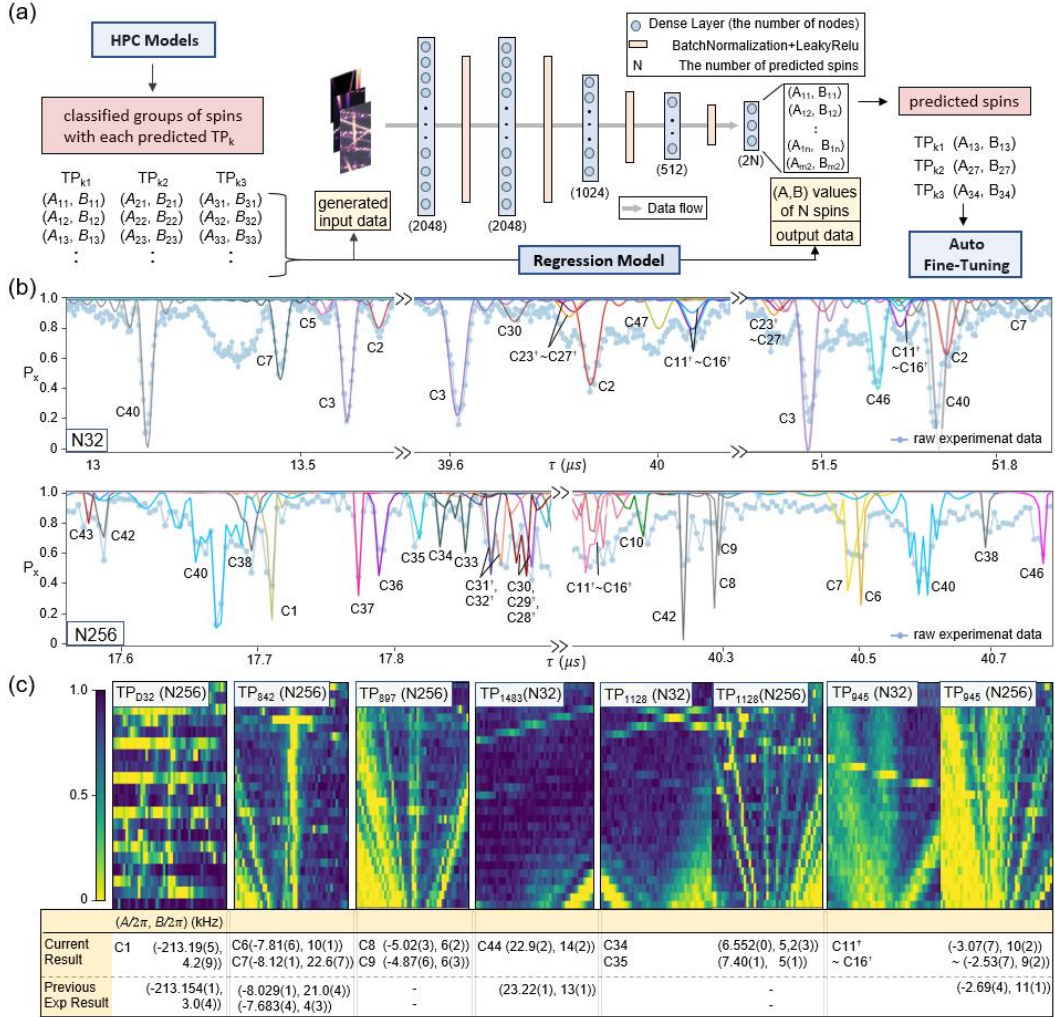


Figure 9. Multiple nuclear spin detection from experimental data. (a) Procedures for tuning hyperfine parameters from predicted periods by HPC models. Training datasets of the regression model are generated using (A, B) pairs with the predicted period by HPC models. The regression model infers the single (A, B) pair that best fits with the features of the experimental data (reorganized as 2D image) including coherence dip amplitudes, envelop function, and fringe patterns. (b) Multiple nuclear spin detection from the experimental CPMG data for $N=32$ (top panel) and $N=256$ (bottom panel) using the same NV center. The panels show superimposed reproduced CPMG signal (solid curves) and the experimental data (dotted curve). The spin numbers ($C\#$) indicated in the figure corresponds to the full spin list summarized in Table S2. (c) Confirmation of detected hyperfine parameters for spins with large number of interfering signatures (1st panel), similar target periods (2nd and 3rd panels), weak local period signature (4th panel), small transverse hyperfine coupling (5th panel), and small longitudinal hyperfine coupling (6th panel). We compare the obtained values to the results of Ref. [32] (bottom row). The panels also show examples of spins with small A that were not detected in Ref. [32] (3rd, 5th, and 6th panels). The order of deviations in parentheses is the same as the order of the last digit of each (A, B) value. The color scale bar in all 2D images ranges from 0 to 1.

3.4 Fully connected based model for regression and fine-tuning step

We now discuss the final stage of the deep learning protocol and the application of the overall procedure to experimental dynamical-decoupling spectroscopy signals as shown in Fig. 9 (a). After application of denoising and HPC models to predict possible local periods, we further apply a deep learning-based regression model to restrict the candidate hyperfine parameters for a subsequent fine-tuning process. Since the period information from HPC model only provides one functional relation between A and B given as Eqn (4), the purpose of the regression model is to find specific (A, B) values that best explain the shape of the coherence dips as a function of τ . We set a search region for the value B ranging from 10 to 70 kHz for N32 (2 to 15 kHz for N256) and find the best fitted (A, B) pairs repetitively for all predicted periods. Since these values are obtained by fitting coherence dips stemming from individual nuclear spins, we use the deep learning-based fit results as an initial guess and iteratively tune (A, B) pairs again in the final step to automatically search a collective list of best fitted (A, B) pairs. We describe a pseudo-code of the fine-tuning method in the Note S7.

3.5 Comparison with previous experimental result

We demonstrate the performance of the developed procedures with two experimental datasets with $N = 32$ and $N = 256$. These new datasets were collected following the methods described in the Ref. [35] and in Figure S4. Figure 9 (b) shows the comparisons of the experimental data to the reproduced CPMG signal using predicted hyperfine parameters by our deep learning protocol. Panels in Fig. 9 (c) show example cases of predicted spins along with corresponding raw experimental data. The first panel

highlights the case where the model can capture the nuclear spin signal and determine $(A, B)/2\pi = (-213.19(5), 4.2(9))$ (kHz) even with overlapping signals stemming from other spins. The second and third panel show that the model can accurately distinguish spins with similar periods and automatic fine tuning successfully identifies individual (A, B) pairs matching the experiments.

Our analysis returns a total of 48 nuclear spins that together accurately describe the data. However, several of these spins yield near-identical hyperfine parameters. It cannot be excluded that those signals originate from a single spin with a broadened signal due to dephasing and nuclear-nuclear spin interactions, which are not included in the model used here (see Note S2 and Figure S5-S7 for details). We anticipate that improved selectivity in this regime is possible by using other pulse sequences, for example non-equally spaced dynamical decoupling sequence [49, 62] or by taking nuclear-nuclear interactions into account. Here, we chose to count groups of spins with nearly identical parameters as a single spin. In that way, we identify 31 nuclear spins. We summarize the full list of detected nuclear spins and the confidence levels in Table S2.

We compare our result with those obtained by other methods on the same sample. A manual analysis on a similar data set, taken with the same measurement procedure, identified 7 spins with parameters that match closely to 7 of the 31 spins identified here [35]. The large improvement in number of identified spins from equivalent experimental data highlights the advantage of our deep learning approach. Additionally, we compare the results to a recent multi-dimensional spectroscopy characterization [32], a more demanding experimental technique that accesses nuclear-nuclear interactions. For 23 of the 31 spins a good match is observed (Table S2). The

other 8 spins were not previously identified and are in a spectral range that was not accessed in the other experiments. We corroborate the identification of these spins through additional experiments with a different number of decoupling pulses $N = 96$ and $N = 128$ (see Figure S8). These results show the capability of our deep learning protocol to automatically and accurately identify nuclear spins in complex spin systems and characterize the coupling parameters from dynamical decoupling spectroscopy.

We estimate a total computational time of 2~3 hours from generating training datasets and training the HPC models to complete the analysis on one set of experimental CPMG data (see details in Figure S2). Once trained, each HPC model can identify the most probable local periods of nuclear spins from the experimental CPMG data almost instantaneously (< 1 second) and obtain the final fitted hyperfine parameters within 40 ~ 50 seconds per spin (detailed specifications of the computational power used is given in Note S2). This fast data analysis highlights the potential of deep learning approaches to efficiently scale up the sensing and characterization of large spin systems.

Chapter 4. Discussion

We find that examining dynamical decoupling spectroscopy signals for various numbers of pulses N is important for the following reasons. First, large N makes spins with small B values visible and this is in general reflected in increased number of detected spins as shown in the fifth panel of Fig. 9 (c), for example. Second, we find that some spins near the Larmor frequency with relatively high B values ($> 10\text{kHz}$) are detectable only in $N = 32$ since for larger N too many spin signals are overlapped as illustrated in the sixth panel of Fig. 9 (c). The current protocol does not take nuclear – nuclear spin interactions into account. Therefore, our model fails to detect some of the interacting nuclear spins for $N = 256$, as for large N and long total evolution times, nuclear-nuclear spin interactions are non-negligible and lead to a deviating period in the signal (see Figure S9 and note that part of the nuclear-nuclear interactions are known from Ref. [32]). For $N = 32$, the data approximately follows a simple electron-nuclear interaction model and nuclear-nuclear interactions can be neglected. In that case, our protocol successfully detects these spins as shown in the fourth panel of Fig. 9 (c). We envision future improvement of the deep learning protocol by taking into account the nuclear – nuclear interactions and building a single unified model which covers all ranges of hyperfine parameters and various N pulse sequences. At this current stage, discrepancies between experimental data for different N , for example between $N = 32$ and $N = 256$, can be used as a signature of nuclear – nuclear interaction.

In conclusion, we have proposed and demonstrated a deep learning approach to automatically detect and characterize individual nuclear spins based on dynamical decoupling spectroscopy with a single electron spin sensor. We have tested the method

on a single NV center in diamond and have identified 31 individual ^{13}C nuclear spins with a wide range of hyperfine parameters. Our method is able to distinguish spins with strong couplings to the NV center which are difficult to handle for conventional peak detection algorithms [63]. Our methodology retains the general benefits of deep learning models; it is easy to modify the training sequence or neural network structures for other types of experimental data such as spectroscopy data of other defect centers in diamond. Additionally, these results highlight the capacity of deep learning algorithms to efficiently analyze the complex nonlinear signatures in nano-scale and single-spin magnetic resonance and its robustness against realistic distortions, such as experimental decoherence and noise. Therefore, our results pave the way for quantum sensing experiments on more complex spin structures and for larger quantum registers and quantum networks based on spin qubits.

Chapter 5. Supporting Information

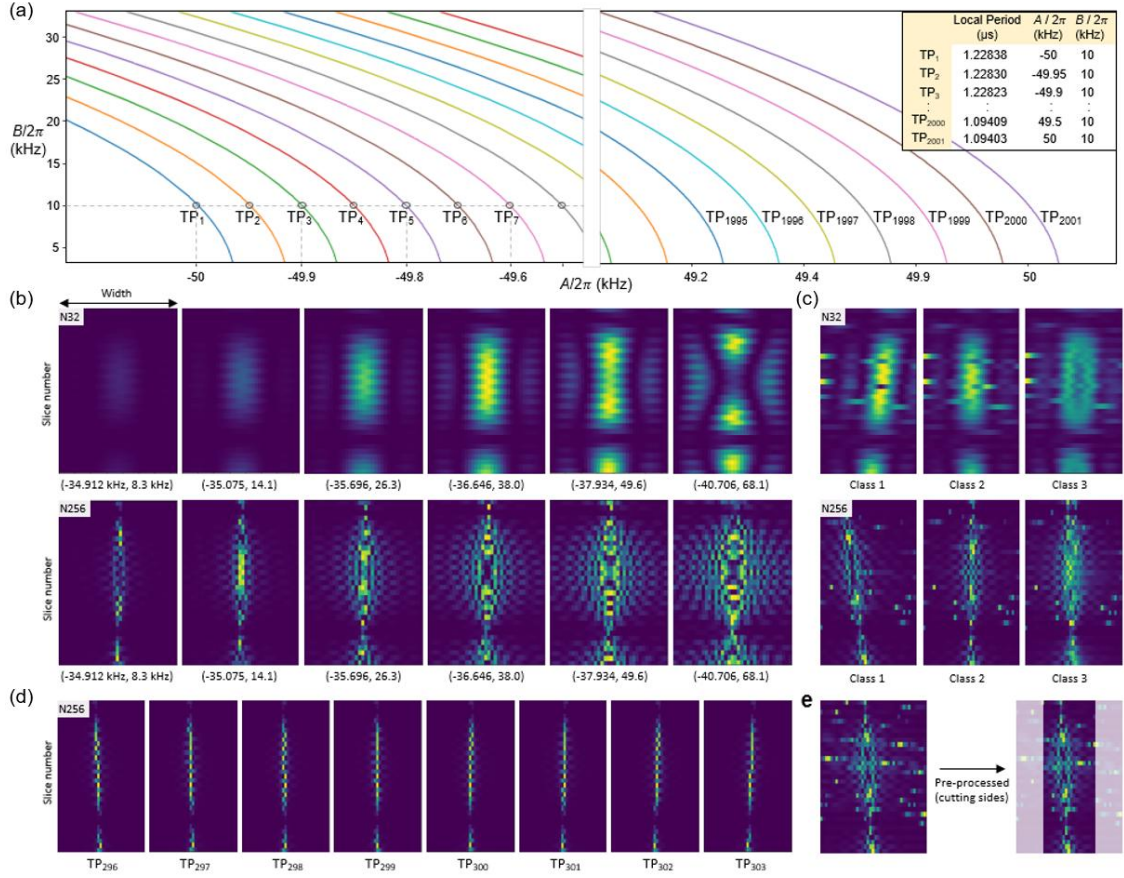


Figure S1. Range of hyperfine parameters (A, B) used for proposed models. (a) Contour lines of local periods (TP_k) in the (A, B) - plane. All (A, B) pairs on one contour line have the same local period but show different fringe patterns. For each hyperfine parameter classifier (HPC) model, the training dataset is generated by using (A, B) pairs on each TP_k curve. For example, the inset table displays TP s calculated with (A, B) values at black circled points using the Eqn. (4) in the main text. (b) Variation of central dips and oscillatory fringe patterns change depending on (A, B) values in the group TP_{300} for pulse repetition $N = 32$ (top row) and $N = 256$ (bottom row). From left to right panels, the local period of each panel remains the same while B value increases, showing more complicated characteristics. (c) Example input images for no, single, and double target spins in HPC model for (A, B) values in group TP_{300} . (d) Panels from left to right show the slope for a single nuclear spin ($A: -34.85$ kHz, $B: 6$ kHz) as a function of varying target periods in step of 50 Hz in A (from TP_{296} to TP_{303}). The width of all images in b, c and d panels is 140 ns and the total number of slices is 33. The colour scale bar in all the images ranges from 0 to 1. (e) Data pre-processing by cutting both sides of an image for HPC models to improve the classification performance and to reduce computational cost.

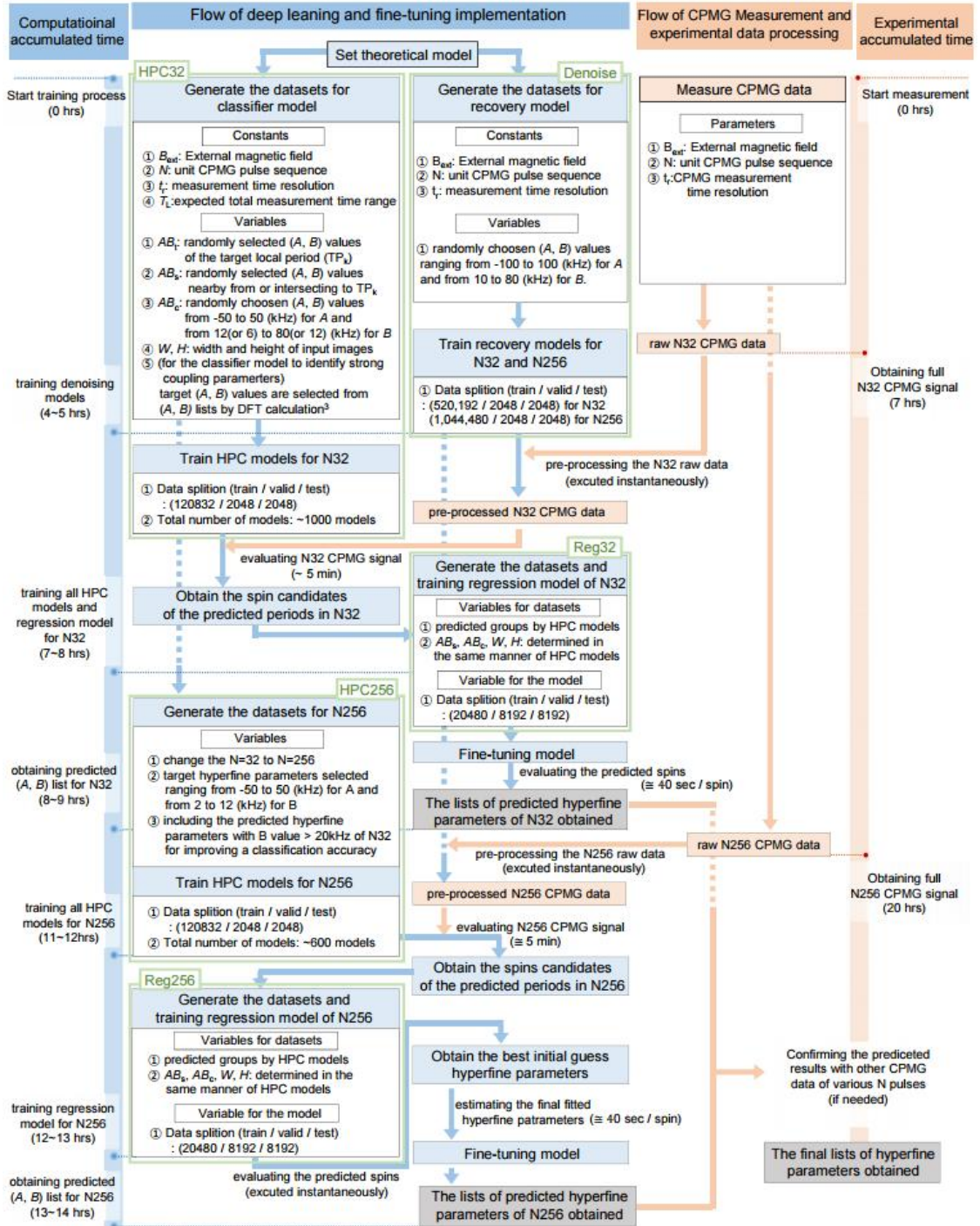


Figure S2. Flow chart of the deep learning protocol and experimental CPMG measurement. The total procedure has two main streams; one is for preparing datasets and training proposed models (blue stream) and the other is for measuring experimental CPMG signals (pink stream). The timeline displayed in left and right sides are the total accumulated time for each flow. Each essential step is marked by light-green rectangular boxes denoted as Denoise, HPC32(256), and Reg32(256). Details are described in Note S2.

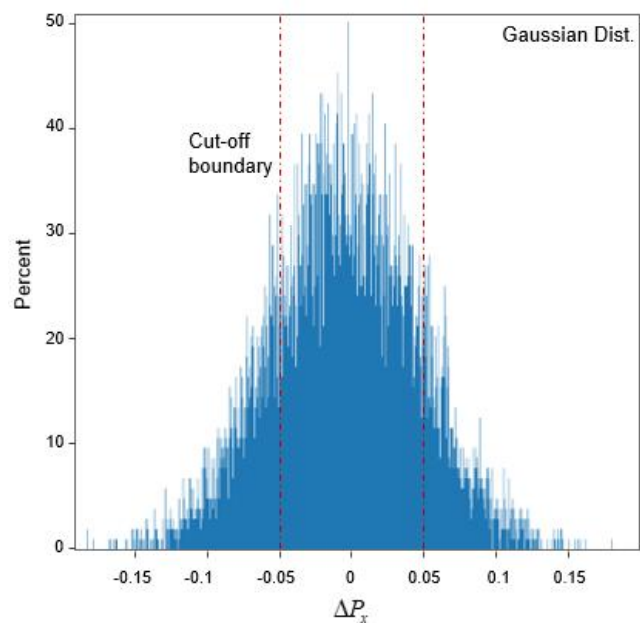


Figure S3. Histogram of the Gaussian distribution used for generating noisy training datasets. This reflects the noise of the experimental data; a cut-off boundary with amplitude of 0.05 measured from the CPMG experimental data is used.

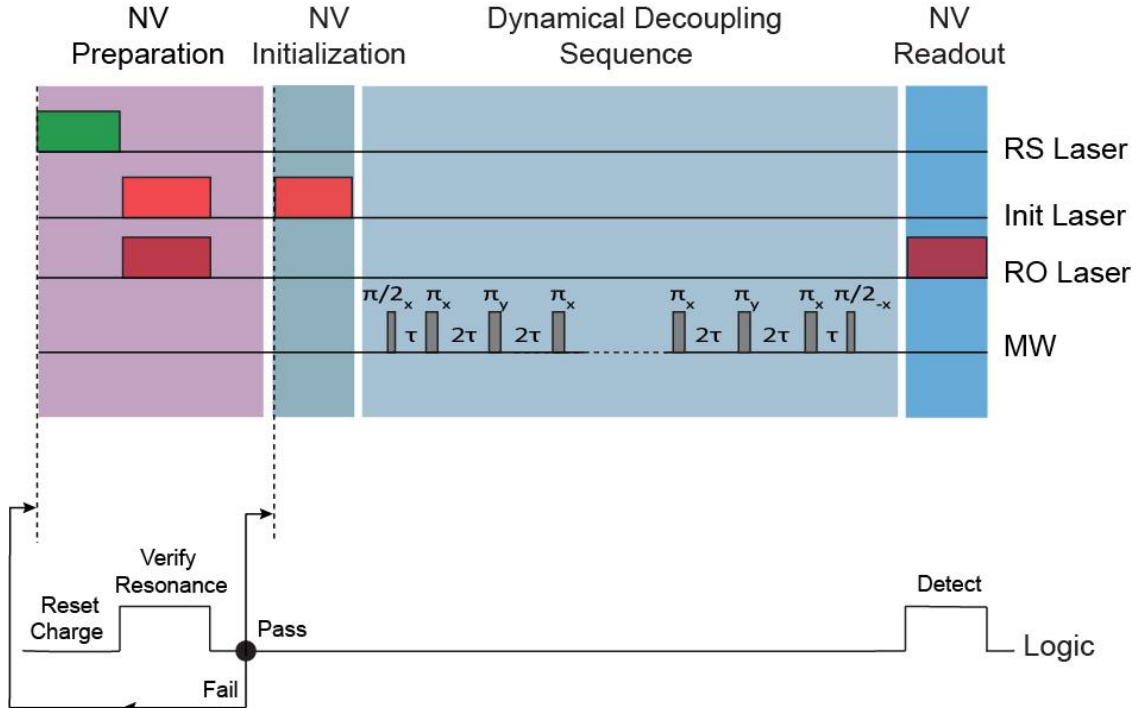


Figure S4. Experimental sequence. The pulse sequence consists of four main parts: NV Preparation, NV Initialization, Dynamical Decoupling Sequence, NV Readout. **NV Preparation:** first the NV centre is prepared in the negative charge state and brought on resonance with the lasers used for the initialization (Init) and Readout (RO) steps. We simultaneously apply the Init and RO lasers for 150 μs and count the number of detected photons (wavelength ~ 637 nm, RO laser resonant with the E_x transition and Init laser resonant with the E' transition) [1]. If the number of detected photons exceeds a certain threshold, the NV is in the negative charge state and on resonance with both lasers, and the sequence proceeds to the next step. If not, the charge reset laser (RS, wavelength ~ 515 nm) is applied for 1 ms and the same process is repeated until success [1]. **NV Initialization:** we initialize the NV electron spin into the $m_s = 0$ state through spin pumping into the E' transition (Init laser, 100 μs) [1]. **Dynamical Decoupling Sequence:** the electron spin is prepared into a superposition state by applying a $\pi/2$ -pulse. Afterwards, a sequence of N π -pulses is applied on the electron spin with the form $(\tau - \pi - \pi)^N$. To reduce the effect of pulse errors, we alternate the phases of the π -pulses according to the XY-8 scheme [2]. **NV Readout:** we apply the RO laser for 10 μs and count the number of detected photons in this period. This allows us to read out the NV electron spin state in a single shot (Fidelity $\sim 94.5\%$).

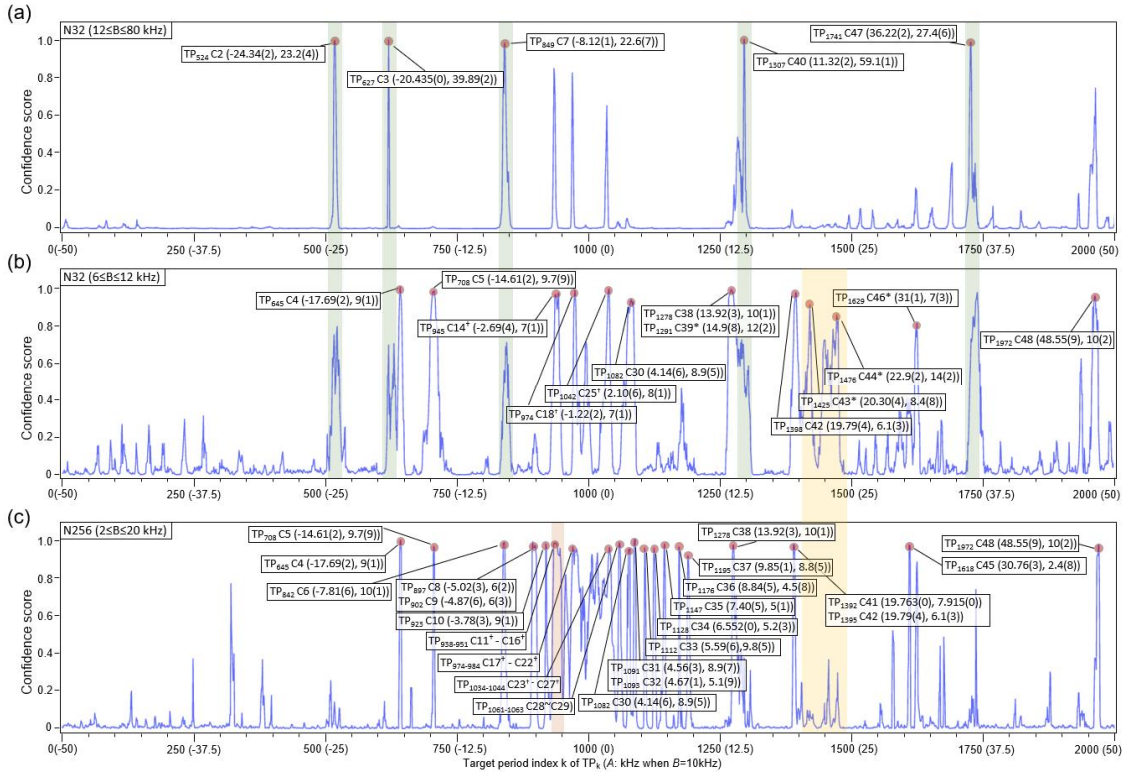


Figure S5. Results from HPC models. (a) Confidence score for N32 ($B \geq 12$ kHz). (b) Confidence score for N32 ($6 \leq B \leq 12$ kHz). (c) Confidence score for N256 ($2 \leq B \leq 20$ kHz). See Note S2 for discussion on the validity of nuclear spin detection highlighted in green and yellow regions. All data are averaged over 10 iterations of training.

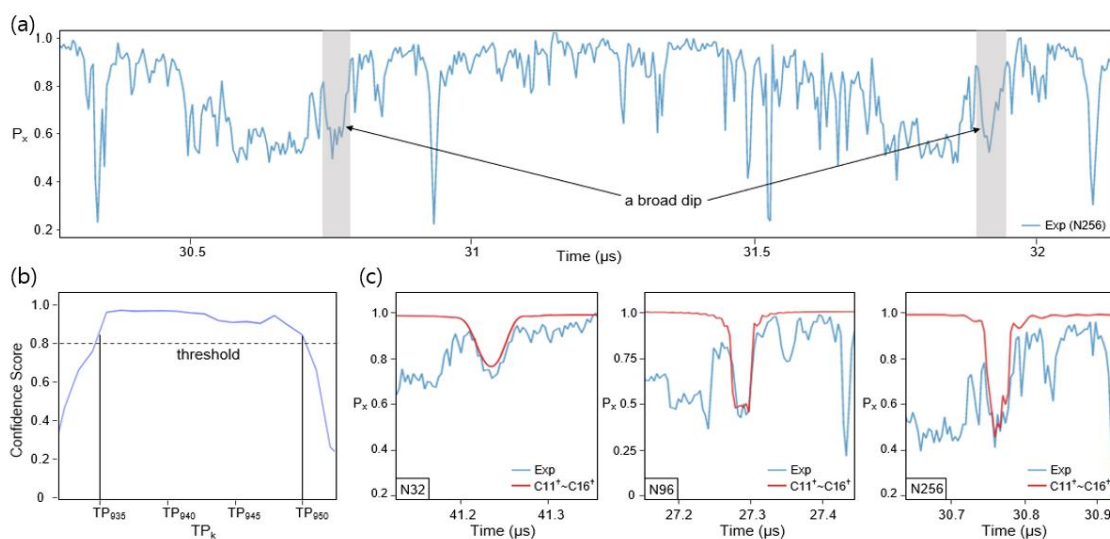


Figure S6. Identifying a group of spins for a single broad dip. (a) A single broad dip (coloured in grey) formed by a group of spins with similar local periods. (b) Confidence scores for the broad dip in the panel a. We note that the confidence scores are higher than the threshold (0.8) for several target period indices. This indicates that such a broad dip might be explained by many spins with similar hyperfine parameters (see Note S2) (c) A comparison of a simulated signal (red line) of $C11^\dagger \sim C16^\dagger$ with the experimental CPMG signal (blue line) for different pulses N32, N96 and N256. More detailed procedures to estimate the number of spins to fit a broad dip are described in Note S2.

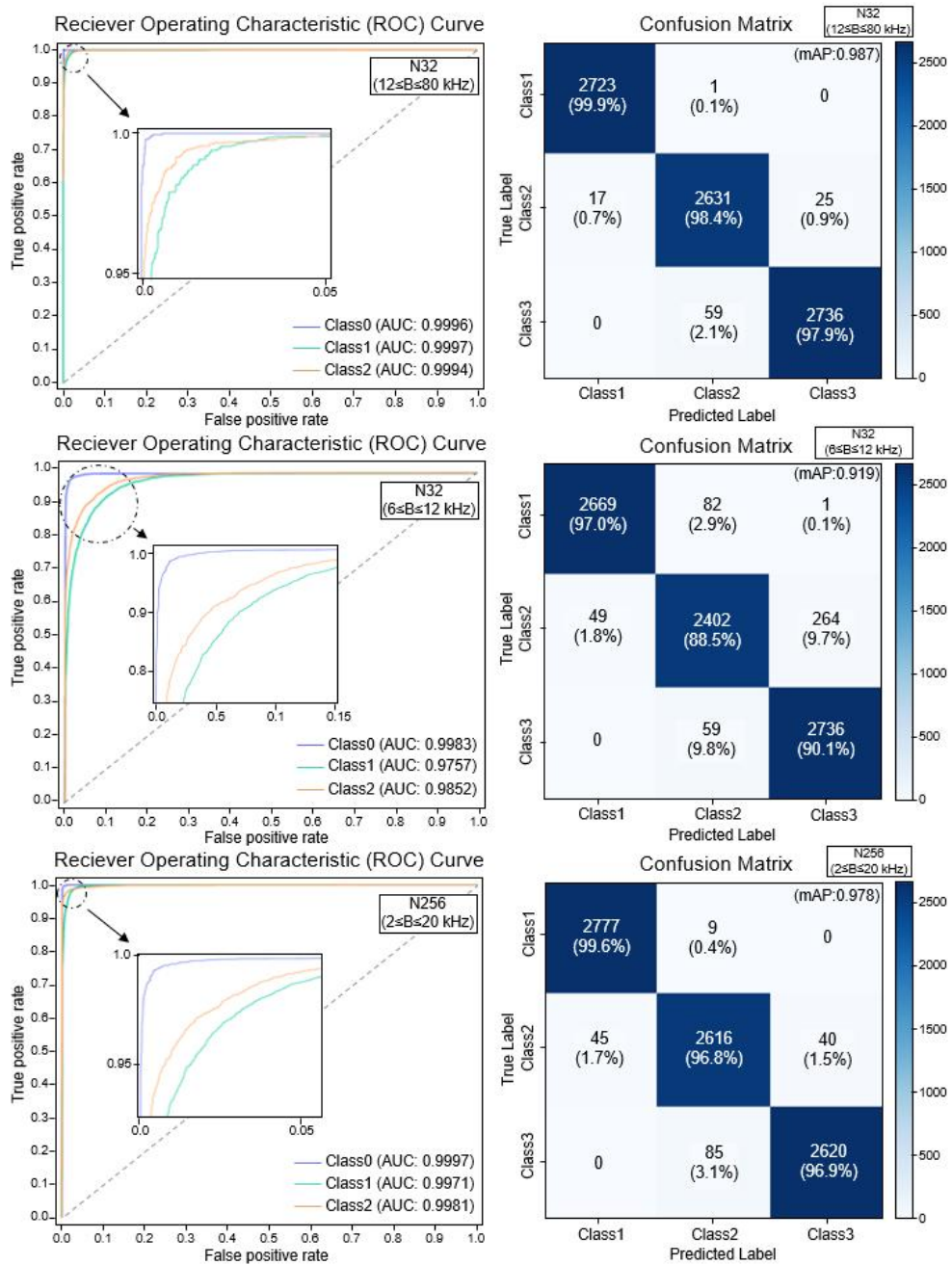


Figure S7. Receiver operating characteristic (ROC) curves and corresponding confusion matrices for HPC models. All the ROC curves and confusion matrices are obtained by averaging the results of all the HPC models which cover the range (unit: kHz) of $-50 \leq A \leq 50$ (for both N32 and N256), $12 \leq B \leq 80$ (the top panel, N32), $6 \leq B \leq 12$ (the second, N32) and $2 \leq B \leq 12$ (the bottom, N256). Each ROC curve is calculated through one-vs-rest class convention. AUC indicates the area under the curve for each class. In confusion matrices, the numbers in boxes indicate the average number of samples and the number in parentheses indicates the ratio of the number of samples to the number of all the true labels for each class. mAP indicates macro-average-precision. The accuracy in the top, the second and the third cases is 98.8%, 95.3% and 97.8% respectively.

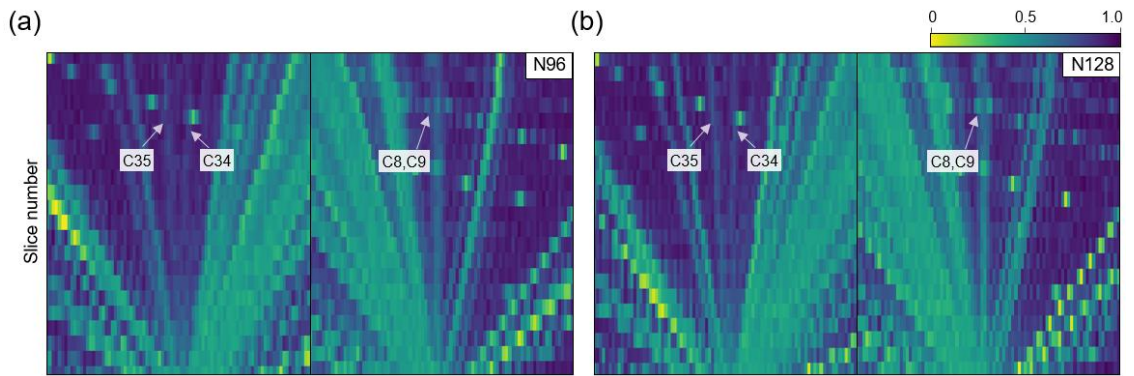


Figure S8. Verification of nuclear spin detection in $N=96$ and $N=128$. In N256 signal, we detect several nuclear spins that were not observed in previous work on the same NV center sample [3] (see Table S2) and confirm some cases using different N pulses. Each panel shows examples using (a) $N = 96$ and (b) $N = 128$ CPMG data. The width of all images is 100 ns and the total number of slices is 22.

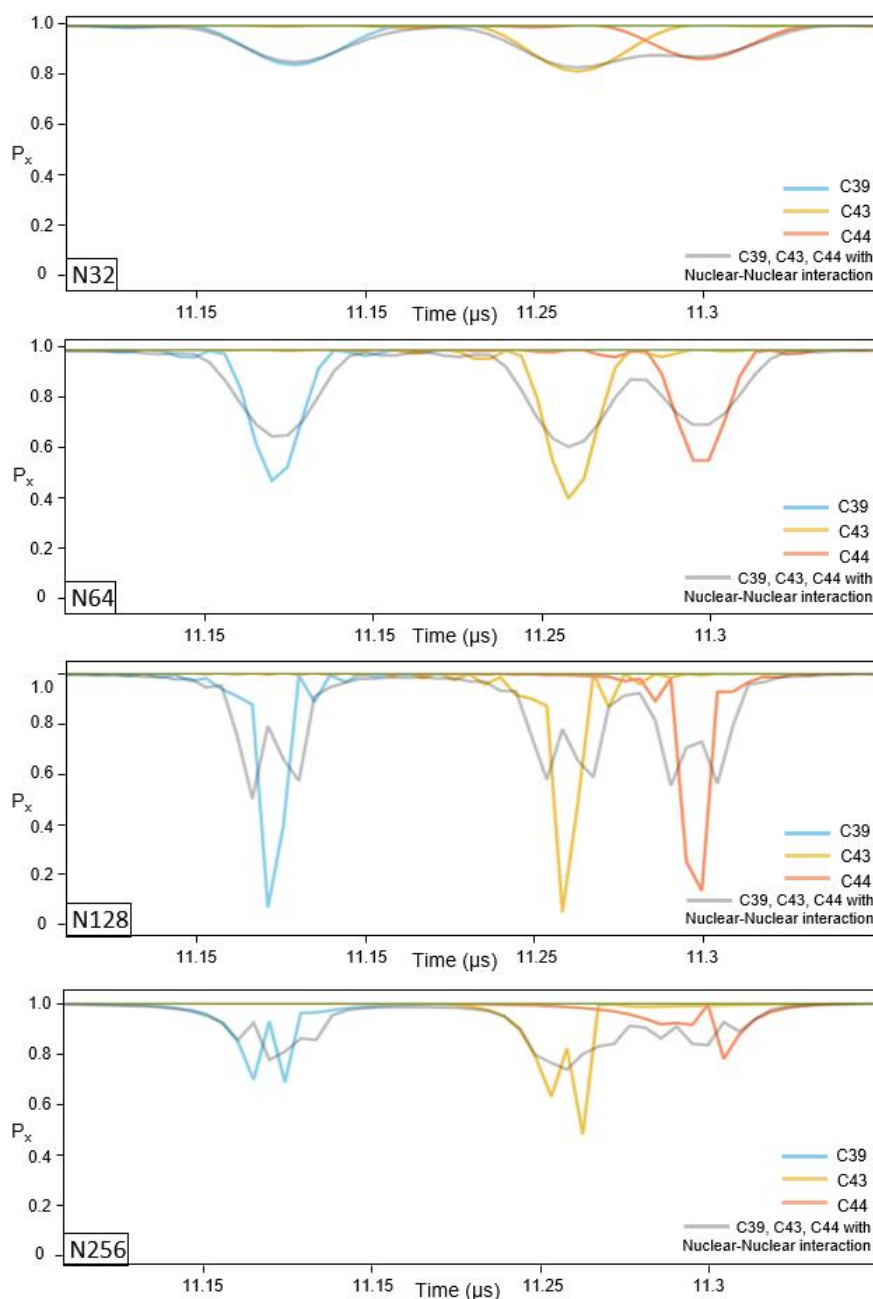


Figure S9. Comparison of CPMG signals with or without nuclear-nuclear interaction. Top to bottom panels: The effect of nuclear-nuclear interaction on CPMG signal for $N = 32$ to $N = 256$ pulse sequences. Blue, yellow, and red lines are simulated by the current theoretical model and a grey line is drawn from a preliminary model including nuclear-nuclear interaction. For example, for a case of C43* and C44* in Figure S5b and 5c, confidence scores covered with a light-yellow bar shows high confidence scores in N32 ($6 \leq B \leq 12$ kHz) but low in N256 ($2 \leq B \leq 20$ kHz). The nuclear-nuclear coupling in this case are set to 236 Hz, 62 Hz and 25 Hz. These are representative values for nuclei with large couplings, to highlight the effect. Typical nuclear-nuclear interactions in the cluster are much smaller [3].

Table S1. Rearranged DFT lists from the Ref.5 according to the target periods used for HPC models. The DFT list are used to build the HPC models for identifying target spins in the strong coupling regime and for generating training datasets for all the HPC models.

	W_h (Hz)	$A/2\pi$ (Hz)	$B/2\pi$ (Hz)		W_h (Hz)	$A/2\pi$ (Hz)	$B/2\pi$ (Hz)
TP_{D1}	138,446,962	137,000,000	19,964,000	TP_{D11}	1,233,552	-1,189,200	327,800
	138,434,443	137,000,000	19,877,000		1,221,358	-1,176,100	329,400
	138,418,692	137,000,000	19,767,000		1,216,771	-1,171,700	328,100
TP_{D2}	12,431,771	12,374,000	1,197,100	TP_{D12}	1,200,629	-1,154,900	328,200
	12,400,753	12,342,000	1,205,700		1,195,339	-1,149,200	328,900
	12,370,525	12,313,000	1,191,600		1,027,859	-890,400	513,500
	12,304,586	12,248,000	1,178,700	1,027,147	-889,000	514,500	
	12,291,453	12,233,000	1,197,300	1,025,671	-887,700	513,800	
	12,239,598	12,183,000	1,175,700	TP_{D13}	1,003,303	-1,003,200	14,400
TP_{D2}	11,322,658	11,225,000	1,483,900		1,001,214	-1,001,100	15,100
	11,269,549	11,174,000	1,464,400		1,000,698	-1,000,600	14,000
	11,225,421	11,128,000	1,475,700	1,027,430	1,019,600	126,600	
TP_{D4}	8,558,610	-8,518,900	823,500	TP_{D14}	996,583	989,100	121,900
	8,545,862	-8,506,700	817,200		975,012	967,500	120,800
	8,524,649	-8,484,400	827,400	TP_{D15}	803,861	577,000	559,700
TP_{D5}	6,444,101	-6,375,600	937,100		795,511	566,100	558,900
	6,438,061	-6,370,200	932,300	792,101	559,900	560,300	
	6,425,047	-6,356,900	933,300	TP_{D16}	753,733	747,400	97,500
	6,407,404	-6,338,300	938,500		752,621	746,200	98,100
	6,406,927	-6,338,600	933,200		749,383	743,000	97,600
	6,402,785	-6,334,000	936,000		744,679	738,400	96,500
TP_{D6}	4,095,934	4,011,700	826,400	739,368	733,200	95,300	
	4,088,638	4,002,800	833,400	737,544	731,400	95,000	
	4,087,828	4,003,300	827,000	TP_{D17}	746,271	720,100	195,900
TP_{D7}	3,697,445	3,621,900	743,600		742,851	716,800	195,000
	3,666,976	3,591,100	742,100	721,552	695,400	192,500	
	3,666,267	3,589,900	744,400	TP_{D18}	665,205	643,300	169,300
	3,657,002	3,580,500	744,100		662,828	641,000	168,700
	3,645,855	3,569,800	740,800		661,556	639,500	169,400
	3,638,169	3,561,200	744,400		TP_{D19}	634,404	603,400
TP_{D8}	2,008,776	1,994,900	235,700	626,457		595,400	194,800
	2,004,365	1,990,600	234,500	625,406		593,900	196,000
	1,991,401	1,977,700	233,200	619,048		587,500	195,100
	1,988,363	1,974,700	232,700	596,823		565,300	191,400
	1,978,570	1,964,600	234,700	592,530		560,800	191,300
	1,954,927	1,941,100	232,100	TP_{D20}	540,330	535,100	75,000
TP_{D9}	1,684,147	1,670,700	212,400		529,272	524,200	73,100
	1,670,334	1,656,800	212,200		512,548	507,800	69,600
	1,669,221	1,655,200	215,900	TP_{D21}	470,843	381,900	275,400
TP_{D10}	1,430,610	-1,424,600	131,000		470,077	381,100	275,200
	1,413,944	-1,407,900	130,600	470,018	381,100	275,100	

	1,391,684	-1,385,400	132,100		468,415	379,700	274,300
<i>TP</i> _{D11}	1,235,815	-1,191,300	328,700		466,611	377,400	274,400
<i>TP</i> _{D22}	458,262	-228,900	397,000	<i>TP</i> _{D32}	204,419	-204,400	2,800
	457,131	-226,100	397,300		203,817	-203,800	2,600
	454,964	-224,000	396,000		202,222	-202,200	3,000
<i>TP</i> _{D23}	463,963	373,900	274,700	<i>TP</i> _{D33}	192,222	-172,800	84,200
	416,703	354,700	218,700		190,784	-171,100	84,400
	416,330	354,200	218,800		186,980	-167,100	83,900
	414,027	351,800	218,300	<i>TP</i> _{D34}	178,944	153,000	92,800
<i>TP</i> _{D24}	376,186	344,900	150,200		178,910	152,900	92,900
	372,716	341,200	150,000	178,327	152,400	92,600	
	370,439	338,400	150,700	<i>TP</i> _{D35}	177,941	-144,600	103,700
<i>TP</i> _{D25}	310,617	-204,500	233,800		177,929	-144,800	103,400
	309,828	-203,300	233,800		177,778	-144,400	103,700
	309,329	-203,000	233,400		177,127	-144,100	103,000
	309,319	-203,100	233,300		177,103	-144,000	103,100
	308,639	-201,600	233,700		176,755	-143,500	103,200
	308,271	-201,500	233,300	<i>TP</i> _{D36}	178,449	-177,100	21,900
<i>TP</i> _{D26}	298,391	291,000	66,000		178,027	-176,700	21,700
	295,324	287,900	65,800		176,737	-175,400	21,700
	294,446	287,000	65,800		176,043	-174,700	21,700
<i>TP</i> _{D27}	272,905	224,200	155,600		174,803	-173,400	22,100
	272,002	223,100	155,600	174,393	-173,000	22,000	
	267,791	219,500	153,400	<i>TP</i> _{D37}	167,740	95,500	137,900
	266,832	218,400	153,300		167,672	96,100	137,400
	265,976	217,000	153,800		167,487	95,200	137,800
	265,790	216,700	153,900		167,126	95,000	137,500
<i>TP</i> _{D28}	259,997	-193,100	174,100		166,956	94,700	137,500
	259,239	-192,800	173,300	166,791	94,700	137,300	
	258,956	-192,600	173,100	<i>TP</i> _{D38}	164,118	-2,400	164,100
<i>TP</i> _{D29}	246,006	243,100	37,700		164,013	-2,100	164,000
	245,732	242,900	37,200		163,600	300	163,600
	245,086	242,200	37,500		163,501	-500	163,500
	245,002	242,100	37,600		163,400	-300	163,400
	243,786	240,900	37,400		163,303	-1,000	163,300
	243,444	240,600	37,100	<i>TP</i> _{D39}	162,651	-151,100	60,200
<i>TP</i> _{D30}	214,134	169,000	131,500		162,205	-150,500	60,500
	213,363	168,100	131,400		161,185	-149,400	60,500
	211,617	165,800	131,500		161,110	-149,400	60,300
<i>TP</i> _{D31}	208,668	97,100	184,700	159,219	-147,400	60,200	
	208,563	96,300	185,000	158,610	-146,700	60,300	

	207,385	94,700	184,500		154,920	28,900	152,200
<i>TP_{D32}</i>	207,115	-207,100	2,500	<i>TP_{D40}</i>	154,067	26,900	151,700
	206,516	-206,500	2,600		153,994	25,900	151,800
	205,416	-205,400	2,600		153,927	25,500	151,800

<i>TP_{D40}</i>	153,152	23,100	151,400	<i>TP_{D47}</i>	110,990	53,400	97,300
	152,653	17,900	151,600		110,235	52,000	97,200
<i>TP_{D41}</i>	142,405	86,400	113,200	<i>TP_{D48}</i>	110,229	51,800	97,300
	142,004	86,000	113,000		110,047	51,600	97,200
	141,245	83,800	113,700		109,954	51,400	97,200
<i>TP_{D42}</i>	137,758	-87,500	106,400	<i>TP_{D49}</i>	97,219	78,900	56,800
	137,631	-87,300	106,400		96,998	78,700	56,700
	137,013	-86,200	106,500		96,894	78,500	56,800
	136,762	-85,800	106,500		96,858	78,600	56,600
	134,944	-83,000	106,400		96,615	78,300	56,600
	134,839	-82,700	106,500		94,744	75,300	57,500
<i>TP_{D43}</i>	133,795	-39,600	127,800	<i>TP_{D50}</i>	94,390	74,700	57,700
	133,736	-39,400	127,800		94,188	74,600	57,500
	133,647	-39,100	127,800		90,478	71,300	55,700
	133,436	-37,700	128,000		93,679	-92,800	12,800
	133,358	-38,100	127,800		93,253	-92,300	13,300
	133,081	-37,800	127,600		92,348	-91,400	13,200
<i>TP_{D44}</i>	128,291	122,900	36,800	<i>TP_{D45}</i>	91,981	-91,000	13,400
	128,234	122,900	36,600		91,825	-90,900	13,000
	128,167	122,800	36,700		91,740	-90,800	13,100
<i>TP_{D45}</i>	119,796	49,700	109,000	<i>TP_{D45}</i>	90,316	-36,300	82,700
	119,648	50,000	108,700		90,265	-36,400	82,600
	119,622	49,500	108,900		90,082	-36,400	82,400
	119,614	49,700	108,800		88,359	68,100	56,300
	119,557	50,000	108,600		88,064	67,800	56,200
	119,531	49,500	108,800		87,361	66,800	56,300
<i>TP_{D46}</i>	119,496	100,400	64,800	<i>TP_{D45}</i>	86,838	66,200	56,200
	119,130	99,900	64,900		86,621	66,000	56,100
	118,706	98,800	65,800		86,176	65,500	56,000
	118,552	99,600	64,300		83,991	65,400	52,700
	118,468	99,500	64,300		83,913	65,300	52,700
	118,373	98,400	65,800		82,548	71,300	41,600
<i>TP_{D47}</i>	118,475	114,100	31,900	<i>TP_{D45}</i>	82,498	71,300	41,500
	116,827	112,500	31,500		82,448	71,300	41,400
	116,758	112,400	31,600		82,118	-47,900	66,700
<i>TP_{D46}</i>	114,455	73,900	87,400	<i>TP_{D45}</i>	82,082	-47,700	66,800
	114,274	73,500	87,500		81,897	-47,800	66,500
	114,262	73,600	87,400		81,587	-46,700	66,900

	114,145	73,300	87,500		81,490	-47,100	66,500
	114,069	73,300	87,400		79,884	-26,100	75,500
	113,992	73,300	87,300	<i>TP_{D45}</i>	79,855	-26,300	75,400
<i>TP_{D47}</i>	111,038	53,500	97,300				
	110,990	53,400	97,300				

Table S2. The resulting hyperfine parameters (A , B) and corresponding confidence scores of the HPC models. The full list of detected nuclear spins and comparison with an independent previous experiment based on multidimensional spectroscopy (a different experimental method) [3] and a previous manual analysis of DD spectroscopy (the same experimental method) [6] on the same NV center. Hyperfine parameters (A , B) calculated by DFT are denoted as $TP_{D\#}$. Confidence scores using raw (denoised) CPMG data is given. The $C\#$ with an asterisk indicates the spins identified to be strongly coupled with nuclear-nuclear interactions in Ref. [3]. $C\#\dagger$ indicates a group of spins which appear as a single but broad dip in experimental CPMG data. The values (parentheses values) in the second and third columns corresponds to the confidence scores of the raw experimental data (the denoised data). Estimated errors of (A , B) values of the deep learning results are defined by standard deviation of the results with 50 iterations of fine-tuning method. Unlike in reference 3, spins with $B \cong 0$ cannot be detected by the experimental sequence used in this work.

The complete list of results									
	Target Period	HPC model confidence score N32	HPC model confidence score N256	Deep learning results for DD spectroscopy		Previous multi-dimensional spectroscopy [3]		Previous analysis for DD spectroscopy [6]	
				$A/2\pi$ (kHz)	$B/2\pi$ (kHz)	$A/2\pi$ (kHz)	$B/2\pi$ (kHz)	$A/2\pi$ (kHz)	$B/2\pi$ (kHz)
C1	TP_{D32}	None	0.98(0.99)	-213.19(5)	4.2(9)	-213.154(1)	3.0(4)		
C2	TP_{524}	0.95(0.98)	None	-24.34(2)	23.2(4)	-24.399(1)	24.81(4)	-24.4	26
C3	TP_{627}	0.98(0.99)	None	-20.435(0)	39.89(2)	-20.569(1)	41.51(3)	-20.6	43
C4	TP_{645}	None	0.98(0.99)	-17.69(2)	9(1)	-17.643(1)	8.6(2)		
C5	TP_{708}	None	0.89(0.91)	-14.61(2)	9.7(9)	-14.548(3)	10(1)	-14.5	11
C6	TP_{842}	None	0.93(0.99)	-7.81(6)	10(1)	-7.683(4)	4(3)		
C7	TP_{849}	0.98(0.99)	None	-8.12(1)	22.6(7)	-8.029(1)	21.0(4)	-8.1	21
C8	TP_{897}	None	0.85(0.84)	-5.02(3)	6(2)				
C9	TP_{902}	None	0.87(0.88)	-4.87(6)	6(3)				
C10	TP_{923}	None	0.93(0.91)	-3.78(3)	9(1)				
C11 [†]	TP_{936} ~ TP_{950}	None	0.95(0.97)	-3.07(7)	10(2)				
C12 [†]		None	0.97(0.95)	-3.02(3)	9(1)				
C13 [†]		None	0.92(0.96)	-2.82(6)	8(2)				
C14 [†]		None	0.93(0.98)	-2.69(4)	7(1)	-2.69(4)	11(1)		
C15 [†]		None	0.94(0.98)	-2.67(5)	8(2)				
C16 [†]		None	0.94(0.93)	-2.53(7)	9(2)				
C17 [†]	TP_{974} ~ TP_{984}	None	0.94(0.97)	-1.32(7)	8(2)				
C18 [†]		None	0.97(0.99)	-1.22(2)	7(1)	-1.212(5)	13(1)		
C19 [†]		None	0.99(0.99)	-1.12(6)	8(2)				
C20 [†]		None	0.93(0.94)	-0.99(4)	6(2)				
C21 [†]		None	0.92(0.96)	-0.84(4)	8(2)				
C22 [†]		None	0.95(0.95)	-0.81(6)	8(9)				

C23 [†]	TP ₁₀₃₄ ~ TP ₁₀₄₄	None	0.95(0.98)	1.711(5)	7(2)				
C24 [†]		None	0.99(0.98)	1.851(5)	6(2)				
C25 [†]		None	0.99(0.97)	2.10(6)	8(2)				
C26 [†]		None	0.97(0.95)	2.21(3)	8(1)				
C27 [†]		None	0.96(0.97)	2.25(4)	10(2)				
C28 [†]	TP ₁₀₆₃ ~	None	0.94(0.96)	3.12(3)	5(2)				
C29 [†]	TP ₁₀₆₃	None	0.97(0.98)	3.16(1)	3.6(9)	3.177(5)	2(4)		
-	None	None	None	None	None	3.618(5)	0(2)		
-	None	None	None	None	None	3.873(5)	0(4)		
C30	TP ₁₀₈₂	0.91(0.90)	0.88(0.91)	4.14(6)	8.9(5)	4.039(5)	0(3)		
-	None	None	None	None	None	4.225(4)	0(6)		
C31 [†]	TP ₁₀₉₁ ~	None	0.96(0.97)	4.56(3)	8.9(7)				
C32 [†]	TP ₁₀₉₃	None	0.97(0.98)	4.67(1)	5.1(9)	4.66(3)	7(4)		
C33	TP ₁₁₁₂	None	0.95(0.99)	5.59(6)	9.8(5)	5.62(1)	5(2)		
C34	TP ₁₁₂₈	None	0.98(0.99)	6.552(0)	5.2(3)				
C35	TP ₁₁₄₇	None	0.91(0.93)	7.40(1)	5(1)				
-	None	None	None	None	None	8.32(1)	3(5)		
C36	TP ₁₁₇₆	None	0.90(0.98)	8.84(5)	4.5(8)				
C37	TP ₁₁₉₅	None	0.95(0.97)	9.85(1)	8.8(5)	9.79(2)	5(4)		
C38	TP ₁₂₇₈	None	0.91(0.92)	13.92(3)	10(1)	13.961(3)	9(1)		
C39*	TP ₁₂₉₉	0.93(0.91)	0.95(0.97)	14.9(8)	12(2)	14.07(2)	13(1)		
C40	TP ₁₃₀₇	0.99(0.99)	None	11.32(2)	59.1(1)	11.346(2)	59.21(3)	11.4	59
C41 [†]	TP ₁₃₉₂ ~	None	0.93(0.93)	19.763(0)	7.915(0)				
C42 [†]	TP ₁₃₉₅	None	0.98(0.98)	19.79(4)	6.1(3)	19.815(3)	5.3(5)		
C43*	TP ₁₄₀₅	0.91(0.93)	None	20.30(4)	8.4(8)	20.72(1)	12(1)		
C44*	TP ₁₄₆₃	0.83(0.85)	None	22.9(2)	14(2)	23.22(1)	13(1)		
C45	TP ₁₆₁₈	None	0.88(0.91)	30.76(3)	2.4(8)				
C46*	TP ₁₆₃₄	0.92(0.93)	None	31(1)	7(1)	31.25(1)	8(2)		
C47	TP ₁₇₄₁	0.99(0.99)	None	36.22(2)	27.4(6)	36.308(1)	26.62(4)	36.4	25
C48	TP ₁₉₇₂	0.88(0.91)	None	48.55(9)	10(2)	48.58(2)	9(2)	48.7	12

Note S1. Diamond sample preparation

Our experiments are performed on a single, naturally occurring, NV centre in a high-purity chemical-vapor-deposition homoepitaxially grown diamond (type IIa) with a natural abundance of ^{13}C (1.1 %) and a $\langle 111 \rangle$ crystal orientation. To improve the photon-collection efficiency, we fabricate a solid immersion lens on top of the NV center and we use an aluminum-oxide anti-reflection coating layer (grown by atomic-layer-deposition) [64]. We use on-chip lithographically-defined striplines to apply microwave fields for fast driving of the electron spin transitions (Rabi frequency ≈ 14 MHz).

We apply a static magnetic field, $B_z \approx 403$ G, along the NV-axis using a permanent room-temperature neodymium magnet. We stabilize the magnet field strength to < 3 mG [19] and the magnet is aligned to the NV-axis with uncertainty of 0.07° using thermal echo sequences (see ref. [32] for details of the alignment procedure).

Our experiments are performed at a temperature of 3.7 K in a commercial closed cycle cryostat (Montana Cryostation). This enables us to readout the NV electron spin state in a single shot with high fidelity (94.5%), through spin-selective resonant excitation [64] (see detailed pulse sequence in Figure S4). The electron spin relaxation time is $T_1 > 1$ hour [35], the natural dephasing time is $T_2^* = 4.9(2) \mu\text{s}$, the spin-echo coherence time is $T_2 = 1.182(5)$ ms, and the multipulse dynamical decoupling coherence time is $T_2^{\text{DD}} > 1$ s, for an optimized inter-pulse delay 2τ [35].

Note S2. Hyperparameter settings for proposed models

S2.1 HPC model

For preparing training datasets of HPC and regression models, the spins of target period are chosen from (A, B) candidates separately grouped by target periods (see Figure S1 and Note S2). The rest of the spin candidates are randomly selected from a previously published list calculated by DFT [58] and from a range $-50 \text{ kHz} < A < 50 \text{ kHz}$ and $B < 80 \text{ kHz}$ for N32, and $2 \text{ kHz} < B < 15 \text{ kHz}$ for N256 signal (see Figure S2 for more details). The reason to choose this range is that the spins with larger values are already calculated in the DFT list. A range of target periods covered by one model is 250 Hz in N32 and 150 Hz in N256 with an evaluation step size of 50 Hz. (see more detailed parameter usage and performance results in Note S2)

Although a two-dimensional convolution layer is generally employed for image recognition, to boost computational speed while retaining the accuracy and validation loss, we use Dense layers for HPC and regression models. The LeakyRelu activation shows slightly better performance for the convergence to the lower validation loss than using ReLU activation. Batch Normalization layer [57] with $\text{epsilon}=1\text{e-}05$, $\text{momentum}=0.1$ (default values in Pytorch 1.3.1) shows faster convergence to the minimum loss than Dropout regularization. For the last layer, Sigmoid layer generally converges to the higher accuracy than the Softmax layer for our datasets.

Based on the prediction results by the HPC models, the regression model is built and trained. The input data are generated from randomly selected (A, B) values of predicted periods by HPC models and the output data, in this case, are those spin values themselves (Fig. 9 (a)). Then, the regression model is trained to predict (A, B) values of

the input data. The evaluated (A , B) lists for the experimental data are used as initial guess for auto fine-tuning model.

S2.2 Denoising model

Unlike the HPC and regression models, training datasets for denoising models are generated in one dimensional data. The spins are selected in the same way as generating datasets for HPC models. We introduce the auto-encoder structure (Fig. 8 (a)) which is an established structure to encode the distribution of the input data and generate the targeted data. For both encoder and decoder parts, 1D CNN layer and 1D transposed CNN layer are employed rather than RNN layers such as LSTM, GRU layers, which show lower validation errors and faster convergence to the minimum loss. All the kernel size for both CNN layers is 4. In the encoder part, Maxpooling1D layer with kernel size of 2 is used after every single 1D CNN layer. A Batch Normalization layer with default parameters is used between all CNN layers.

In all models, AdaBound [65] is employed for the optimizer and the initial learning rate is 0.00015 decayed at each epoch with customized rate (0.5 ~ 0.25). For loss functions, BinaryCrossEntropy loss is used for HPC model and MeanSquareError loss is used for regression and denoising models.

S2.3 Fine-tuning

For the auto fine-tuning, the objective functions are defined as,

$$Loss = \sum_i^M \sum_{t \in T_i \cup T_{bath}} [g(t) - p(t)]^2 \quad (6)$$

where $g(t)$ is the generated CPMG signal with all predicted (A, B) values, $p(t)$ is the experimental data, T_i is a set of data points near dips of i^{th} spin in the generated data and T_{bath} is a set of data points where spin baths are formed. For number of predicted spins M , the optimization process runs over the $2M$ -dimensional space ($2M$ variables; M for A and M for B independently).

Since the loss function is not convex, instead of adopting the algorithms such as a gradient descent, particle swarm optimization (PSO) [66] is employed for the optimization process. The number of needed particles increases exponentially as search dimensions increase, yielding a large computational cost. To reduce the cost, the optimization process is conducted sequentially only on one pair of (A, B) at once and iterated for every single spin until the total loss is converged because, as in Eqn. (6), the loss function can be split into each term of i^{th} spin candidate. (see pseudo code in Note S7)

S2.4 Usage of trained models and management of total computational time

The denoising model can be reused for other samples if the number of unit CPMG pulse sequence (N) and measurement time resolution are kept the same. The classifier model can be reused if the external magnetic field, N , measurement time resolution, and total measurement time length remain the same.

All HPC and denoising models can be trained separately and generating datasets can also be processed independently. Therefore, for example to reduce total computational time to one-third, three computers can be used independently by dividing the training regions of all TP_k into three regions. More detailed parameter usage and whole procedures for implementations of each model and processing experimental data are described in Figure S2 and Note S2.

Note S3. Detailed procedure of machine learning protocol

S3.1 Denoising model (Annotated as Denoise in Figure S2) – Recovering noisy signals. To generate training datasets for a denoising model, (A, B) pairs are collected in the same way as in HPC models but not pre-processed in the image representation as in Fig.7. We use the gaussian noise distribution with standard deviation 0.05, which reflects the maximum amplitude of experimental noise. (see Figure S3) The length of input data is 12 μ s (3000 data points with 4 ns time resolution in our experimental setup) but the performance of the model does not depend much on the length between 1000 and 3000. The sample datasets and training implementation is described in an online tutorial section; Tutorial part 2 – Denoising model at https://github.com/kyunghoon-jung/Deep_Learning_CPMG_Analysis.

S3.2 HPC model (HPC32, HPC256 in Figure S2) – Identifying local periods

of existing nuclear spins. The target period (TP_k) shown in Figure S1 (a) is calculated with the approximate equation [5],

$$TP_k = 2\pi / (\tilde{\omega}_k + \omega_L) \quad (1)$$

, where $\tilde{\omega}_k = \sqrt{(A_k + \omega_L)^2 + B_k^2}$, ω_L is the Larmor frequency and A_k and B_k are hyperfine parameters of the k^{th} target period. We pre-calculate target periods by a step size of $A = 50$ Hz with a fixed $B (=10$ kHz) value as seen in the inset table in Figure S1 (a) and save it as a Python dictionary file - [key (A values) : value (target periods)]. The evaluation step size is 50 Hz for A . Figure S1 (d) describes how a slope of a central line changes at each step. The data manipulation and the dictionary file are presented in an online tutorial; Tutorial part 1 - Data handling and generation in the proposed representation at the same link above.

The external magnetic field (B_z) is 403.553 G. The measurement time resolution (t_r) of the CPMG signal is 4 ns. The width (W) of the input images sliced by TP_k are reduced to be 80~120 ns for the range of $A \leq -10$ kHz and $A \geq 10$ kHz and to be 40~80 ns for $-10 \leq A \leq 10$ kHz for the optimal performance and reducing the computational cost. (see Figure S1 (e)) The height (H , total number of slices) is determined depending on the total measurement length of the experimental data. The total measurement length of experimental CPMG data of N32 (N256) is 6 ~ 50 μ s (10 ~ 40 μ s).

Spins with different periods from TP_k and spins from the list in Table S1 taken from the density functional theory (DFT) calculation result [58] are included in training

datasets to make the model robust in the presence of other spins with various periods. The total number of spins for generating each input data is randomly selected between 26~32 where 90~100% of the total number of spins are selected from the range $-50 \leq A \leq 50$ kHz, $6 \leq B \leq 80$ kHz for $N = 32$ datasets and $-50 \leq A \leq 50$ kHz, $2 \leq B \leq 20$ kHz for $N = 256$ datasets while the rest 0~10% of the spins are selected from the DFT list. The reason to choose the upper bound as $B = 20$ kHz for $N = 256$ datasets is that the spins with $B \geq 20$ kHz can be evaluated accurately in N32. (see Figure S5 (a) and the top panels in Figure S7) When evaluating the strong coupling regime (for example $\omega_h/2\pi > 80$ kHz), the HPC models only cover the range near the (A, B) values in the DFT list because the distribution of (A, B) values in this regime is distributed sparsely. [58] (also see Table S1).

At first, HPC models are trained with two classes; Class 1 is generated excluding a spin with the target period and Class 2 is generated including a spin with the period. And to reduce computational cost, training datasets consist of multiple target periods so one HPC model is trained to evaluate several target periods. For example, if a model is built with datasets of $TP_{501} \sim TP_{505}$, the model is trained to evaluate five target periods ($TP_{501}, TP_{502}, TP_{503}, TP_{504}$ and TP_{505}). We train one HPC model with 5 target periods for N32 and 3 target periods for N256.

Figure S5 shows confidence scores for N32 and N256 and detected spins circled in red. As shown in Figure S5 (a) and (b), when evaluating the signal of N32, we train the HPC models with two different range of B values to enhance the performance for a range of small B values ($6 \leq B \leq 12$ kHz). In green coloured regions in panel b, spins are not selected although some points show high confidence scores. Because target period

indices of spins with large B values (C2, C3, C7, C40 and C47) are overlapped in this region as seen in panel a, b.

To extract predicted periods of high confidence scores (see red circles in Figure S5), we use the 'find_peaks' function (a signal processing function of scipy package in Python) with parameters of height=0.75(N32, $6 \leq B \leq 12\text{kHz}$) and 0.9(N32, $B \geq 12\text{kHz}$ and N256), distance=4, width=2, prominence=0.5. The classification resolution is $A = 500$ Hz for N32 ($6 \leq B \leq 12$ kHz), $A = 200$ Hz for N32 ($B \geq 12$ kHz) and $A = 150$ Hz for N256 of $B \leq 20\text{kHz}$; a classification resolution means the minimum difference where two different nuclear spins can be accurately distinguished. See an implementation sample in an online tutorial; Tutorial part 3, 4 – Hyperfine parameter classifier (HPC) model at the same link above.

S3.3. Regression model (Reg32, Reg256 in Figure S2) – Estimating (A , B) values for predicted periods in Note S3.1. Before specifying (A , B) values, we train additional HPC models to determine the number of nuclear spins for the case of a broad dip (see Figure S6). A broad dip in N256 shows confidence scores higher than a threshold in a range of more than four target period indices (see an example in Figure S6 (a) and (b)). The structure of the model remains the same as in Fig.7, but an input dataset is generated with a group of target spins selected within the predicted periods.

For example, in Figure S6 (b), confidence scores of $TP_{935} \sim TP_{950}$ are higher than the threshold. In this case, an output one-hot vector has 5 dimensions where Class 1 [1,0,0,0,0] corresponds to 'No target spin', Class 2 [0,1,0,0,0] corresponds to the number of spins = 4 and Class 3 [0,0,1,0,0] (Class 4 [0,0,0,1,0], Class 5 [0,0,0,0,1]) to the number

of spins = 5 (6, 7) respectively. Heuristically, one spin exists if confidence scores are shown higher than a threshold for 2 ~ 4 target periods. So, for example, if confidence scores are high for 8 target periods (or 13 target periods), then the minimum number of spins to exist is 2 (or 4). This determines the minimum number (=4 in this case because confidence scores are high for $TP_{935} \sim TP_{950}$) of spins for training datasets. The maximum number (=7 in this example) of spins is chosen depending on a classification resolution of the HPC model. The additional HPC model outputs a vector with the highest confidence score in Class 4 which is assigned to the number of spins = 6. (Output vector is [0.00012, 0.00332, 0.2312, 0.6756, 0.3121]) After obtaining the number of spins, the regression step in Fig.9 is performed.

Although the model quantitatively estimates the number of spins, the actual number of spins underlying these broader signals is difficult to be determined, as nuclear-nuclear interactions and dephasing can play a role, and are not taking into account in our model. Therefore, we choose to count a group of spins forming a broad dip (denoted as $C\#^\dagger$ in Table S2) as one spin so that the groups $C11^\dagger \sim C16^\dagger$, $C17^\dagger \sim C22^\dagger$, $C23^\dagger \sim C27^\dagger$, $C31^\dagger \sim C32^\dagger$ and $C41^\dagger \sim C42^\dagger$ are counted as five spins in total (each contains at least one spin). This conservative way of counting reduces the total number of spins from 48 to 31. A more detailed implementation can be found in an online tutorial; Tutorial part 5 – Regression Model at the same link above.

Note S4. Classification performance – ROC curves and confusion matrices

For ROC curves in Figure S7, AUC scores in N32 ($6 \leq B \leq 12$ kHz) are lower than those in other cases because the dips of spins with B ($6 \leq B \leq 12$ kHz) in N32 are less distinct than those with larger B values. The lower bound of B values (6 kHz in N32 and 2 kHz in N256) of HPC models are determined by the minimum amplitudes of dips distinguishable by models. The bounds can be customized for more optimal performances depending on measurement configurations. The confusion matrices show HPC models in N32 ($6 \leq B \leq 12$ kHz) have difficulty distinguishing Class 1 (one target period) and Class 2 (two target periods), which leads to a relatively low classification resolution in this range. Due to this ambiguity in the results of HPC models with this range, we count the number of spins in a conservative way for the case of continuously high confidence scores. For example, an area of high confidence scores within a range of 10 target periods is counted as one spin and for a range of 10~20 target periods the number of spins is estimated as two spins. (see the cases of C38, C39 in Figure S5 (b))

Note S5. Hardware specification and computational time management – The total accumulated computational time is shown in left side of Figure S2. The required time is measured by a workstation with following specifications. CPU: Intel Core i9-9920X (12 cores, 24 threads), RAM: 128GB DDR4, and GPUs: NVIDIA RTX 2080Ti (x2). In the whole procedure, the usage of multi-threads is fixed to 20 threads.

The computational time can be reduced by using multiple computers simultaneously because Step.1 and Step. 2 can be trained independently. In addition, training each HPC model and generating datasets can be implemented independently. The

trained denoising model can be reused for other experimental data sets if the number of CPMG pulse sequence units (N) and measurement time resolution (t_r) are kept the same, while the trained classifier model can be reused when the B_{ext} , N , t_r , and T_L remain the same. (N , t_r , B_{ext} , and T_L are parameters shown in Figure S2)

Note S6. Discussion – Effect of nuclear-nuclear interaction In Figure S5 (b) and (c) (see light-yellow bar), it is shown that C43, C44 has high confidence scores in N32 but not in N256 because nuclear-nuclear interaction turns significant as N pulse increases (see Figure S9). Comparing the top panel (N32) and the bottom panel (N256) in Figure S9, a grey line in N256 shows a small and smooth dip making HPC models fail to detect nuclear spins. In our current theoretical model, nuclear-nuclear interaction is not taken into account. The main difficulty in addressing this nuclear-nuclear interaction lies in computing all the possible interactions between nuclear spin candidates.

Note S7. Pseudo code of the fine-tuning method.

Algorithm 1: Fine Tunning Algorithm

```
Function FineTunning:
  Input: Regression data list  $[(A_i, B_i)], i = 1, 2, \dots, n$ , where HPC values are from regression.
  Output: Processed list.
  for Idx, (A, B) in enumerate(Regression_list) do
    P = Particles.Initialization(Regression_list, Idx, dB, N_particles)
    best_loss = loss(P[0])
    best_particle = P[0]
    for p in P do
      if  $N\_pulse == 32$  then
        | Optimize p with Conjugate Gradient Optimizer.
      else
        | Optimize p with L-BFGS-B Optimizer.
      end
      if  $loss(p) < best\_loss$  then
        | best_loss  $\leftarrow loss(p)$ 
        | best_particle  $\leftarrow p$ 
      else
      end
    end
    Regression_list  $\leftarrow best\_particle$ 
  end
return

Function Particle.Initialization:
  Input: Regression_list, idx, dB, N_particles
  Output: List of the particles.
  Particles = []
  A0 = Regression_list[idx][0]
  B0 = Regression_list[idx][1]
  for B in linspace(B0 - dB, B0 + dB, N_particles) do
    temp_particle  $\leftarrow Regression\_list$ 
    temp_particle[idx]  $\leftarrow (A0, B)$ 
    Particles.append(temp_particle)
  end
return

Function loss:
  Input: Regression_list, Idx, Experiment_data.
  Output: Loss_value.
  for (A, B) in Regression_list do
    OneAB_data  $\leftarrow P(A, B)$ 
    Generated_data  $\leftarrow P(Regression\_list)$ 
    peaks = FindPeaks(OneAB_data, separation = T(A, B))
    /* Each P(A, B) and P(Regression_list) returns generated CPMG signal
       and T(A, B) returns period of P(A, B) */
    Loss_value = 0
    for peak in peaks do
      Loss_value += L2Norm(Generated_data[peak-10:peak+10]
        - Experiment_data[peak-10:peak+10])
    end
  end
return
```

Supplementary Reference

- [1] Robledo, L. et al. High-fidelity projective read-out of a solid-state spin quantum register. *Nature* **477**, 574-578 (2011).
- [2] Gullion, T., Baker, D. B. & Conradi, M. S. New, compensated Carr-Purcell sequences. *J. Magn. Reson.* **89**, 479–484 (1990).
- [3] Abobeih, M. H. et al. Atomic-scale imaging of a 27-nuclear-spin cluster using a quantum sensor. *Nature* **576**, 411-415 (2019).
- [4] Taminiau, T. H. et al. Detection and Control of Individual Nuclear Spins Using a Weakly Coupled Electron Spin. *Phys. Rev. Lett.* **109**, 137602 (2012).
- [5] Nizovtsev, A. P. et al. Non-flipping C-13 spins near an NV center in diamond: hyperfine and spatial characteristics by density functional theory simulation of the C-510[NV]H-252 cluster. *New J. Phys.* **20**, 023022 (2018).
- [6] Abobeih, M. H. et al. One-second coherence for a single electron spin coupled to a multi-qubit nuclear-spin. *Nat. Commun.* **9**, 2552 (2018).

BIBLIOGRAPHY

- 1 T. D. Ladd, F. Jelezko, R. Laflamme, Y. Nakamura, C. Monroe and J. L. O'Brien. "Quantum computers." *Nature* 464, 45–53 (2010).
- 2 A. Streltsov, G. Adesso, and M. B. Plenio. "Colloquium: Quantum coherence as a resource." *Rev. Mod. Phys.* 89, 041003 (2017).
- 3 R. Schirhagl, K. Chang, M. Loretz, and C. L. Degen. "Nitrogen-Vacancy Centers in Diamond: Nanoscale Sensors for Physics and Biology." *Annu. Rev. Phys. Chem.* 65, 83-105 (2014).
- 4 A. M. Souza, G. A. Álvarez and D. Suter. "Robust dynamical decoupling." *Phil. Trans. R. Soc. A* 370, 4748–4769 (2012).
- 5 T. H. Taminiau, J. J. T. Wagenaar, T. van der Sar, F. Jelezko, V. V. Dobrovitski, and R. Hanson. "Detection and Control of Individual Nuclear Spins Using a Weakly Coupled Electron Spin." *Phys. Rev. Lett.* **109**, 137602 (2012).
- 6 K. Bock and C. Pedersen in *Advances in Carbohydrate Chemistry and Biochemistry* Vol. 41 (eds R. Stuart Tipson & Derek Horton) 27-66 (Academic Press, 1983).
- 7 J. M. Tognarelli, M. Dawood, M. I.F. Shariff, V.P.B. Grover, M. M.E. Crossey, I. Jane Cox, S. D. Taylor-Robinson, and M. J.W. McPhail. "Magnetic Resonance Spectroscopy: Principles and Techniques: Lessons for Clinicians." *J. Clin. Exp. Hepatol.* **5**, 320-328 (2015).
- 8 J. M. Wurz, S. Kazemi, E. Schmidt, A. Bagaria and P. Guntert. "NMR-based automated protein structure determination." *Arch. Biochem. Biophys.* **628**, 24-32 (2017).
- 9 P. Guntert, "Automated structure determination from NMR spectra." *Eur. Biophys. J. Biophys.* **38**, 129-143 (2009).
- 10 A. Abbas, X. B. Kong, Z. Liu, B. Y. Jing and X. Gao. "Automatic Peak Selection by a Benjamini-Hochberg-Based Algorithm." *Plos One* **8**, e53112 (2013).
- 11 A. Polanski, M. Marczyk, M. Pietrowska, P. Widlak and J. Polanska. "Signal Partitioning Algorithm for Highly Efficient Gaussian Mixture Modeling in Mass Spectrometry." *Plos One* **10**, e0134256 (2015).
- 12 S. Nerli, A. C. McShan and N. G. Sgourakis. "Chemical shift-based methods in NMR structure determination." *Prog. Nucl. Mag. Res. Sp.* **106**, 1-25 (2018).
- 13 N. Aharon, A. Rotem, L. P. McGuinness, F. Jelezko, A. Retzker and Z. Ringel. "NV center based nano-NMR enhanced by deep learning." *Bioinformatics* **34**, 2590-2597 (2018).

- 14 P. Klukowski, M. Augoff, M. Zieba, M. Drwal, A. Gonczarek, M. J. Walczak. NMRNet: a deep learning approach to automated peak picking of protein NMR spectra. *Sci. Rep.* **9**, 17802 (2019).
- 15 L. Childress, M. V. Gurudev Dutt, J. M. Taylor, A. S. Zibrov, F. Jelezko, J. Wrachtrup, P. R. Hemmer and M. D. Lukin. “Coherent dynamics of coupled electron and nuclear spin qubits in diamond.” *Science* **314**, 281-285 (2006).
- 16 S. Kolkowitz, Q. P. Unterreithmeier, S. D. Bennett, and M. D. Lukin. “Sensing Distant Nuclear Spins with a Single Electron Spin.” *Phys. Rev. Lett.* **109**, 137601 (2012).
- 17 N. Zhao, J. Honert, B. Schmid, M. Klas, J. Isoya, M. Markham, D. Twitchen, F. Jelezko, R. B. Liu, H. Fedder and J. Wrachtrup. “Sensing single remote nuclear spins.” *Nat. Nanotechnol.* **7**, 657-662 (2012).
- 18 F. Shi, X. Kong, P. Wang, F. Kong, N. Zhao, R. B. Liu and J. Du. “Sensing and atomic-scale structure analysis of single nuclear-spin clusters in diamond.” *Nat. Phys.* **10**, 21-25 (2014).
- 19 T. H. Taminiau, J. Cramer, T. van der Sar, V. V. Dobrovitski and R. Hanson. “Universal control and error correction in multi-qubit spin registers in diamond.” *Nat. Nanotechnol.* **9**, 171-176 (2014).
- 20 W. B. Gao, A. Imamoglu, H. Bernien and R. Hanson. “Coherent manipulation, measurement and entanglement of individual solid-state spins using optical fields.” *Nat. Photon.* **9**, 363-373 (2015).
- 21 G. Q. Liu, J. Xing, W. L. Ma, P. Wang, C. H. Li, H. C. Po, Y. R. Zhang, H. Fan, R. B. Liu, and X. Y. Pan. “Single-Shot Readout of a Nuclear Spin Weakly Coupled to a Nitrogen-Vacancy Center at Room Temperature.” *Phys. Rev. Lett.* **118**, 150504 (2017).
- 22 E. Bernardi, R. Nelz, S. Sonusen and E. Neu. “Nanoscale Sensing Using Point Defects in Single-Crystal Diamond: Recent Progress on Nitrogen Vacancy Center-Based Sensors.” *Crystals* **7**, 124 (2017).
- 23 J. Zopes, K. S. Cujia, K. Sasaki, J. M. Boss, K. M. Itoh and C. L. Degen. “Three-dimensional localization spectroscopy of individual nuclear spins with sub-Angstrom resolution.” *Nat. Commun.* **9**, 4678 (2018).
- 24 M. Pfender, P. Wang, H. Sumiya, S. Onoda, W. Yang, D. B. R. Dasari, P. Neumann, X. Y. Pan, J. Isoya, R. B. Liu and Jörg Wrachtrup. “High-resolution spectroscopy of single nuclear spins via sequential weak measurements.” *Nat. Commun.* **10**, 594 (2019).
- 25 R. Nagy, M. Niethammer, M. Widmann, Y. C. Chen, P. Udvarhelyi, C. Bonato, J. U. Hassan, R. Karhu, I. G. Ivanov, N. T. Son, J. R. Maze, T. Ohshima, Ö. O. Soykal, Á. Gali, S. Y. Lee,

- F. K. and J. Wrachtrup. “High-fidelity spin and optical control of single silicon-vacancy centres in silicon carbide.” *Nat. Commun.* **10**, 1954 (2019).
- 26 M. H. Metsch, K. Senkalla, B. Tratzmiller, J. Scheuer, M. Kern, J. Achard, A. Tallaire, M. B. Plenio, P. Siyushev and Fedor Jelezko. “Initialization and Readout of Nuclear Spins via a Negatively Charged Silicon-Vacancy Center in Diamond.” *Phys. Rev. Lett.* **122**, 190503 (2019).
- 27 K. S. Cujia, J. M. Boss, K. Herb, J. Zopes and C. L. Degen. “Tracking the precession of single nuclear spins by weak measurements.” *Nature* **571**, 230–233 (2019).
- 28 C. T. Nguyen, D. D. Sukachev, M. K. Bhaskar, B. Machielse, D. S. Levonian, E. N. Knall, P. Stroganov, R. Riedinger, H. Park, M. Lončar, and M. D. Lukin. “Quantum Network Nodes Based on Diamond Qubits with an Efficient Nanophotonic Interface.” *Phys. Rev. Lett.* **123**, 183602 (2019).
- 29 B. Hensen, W. W. Huang, C. H. Yang, K. W. Chan, J. Yoneda, T. Tantt, F. E. Hudson, A. Laucht, K. M. Itoh, T. D. Ladd, A. Morello and A. S. Dzurak. “A silicon quantum-dot-coupled nuclear spin qubit.” *Nat. Nanotechnol.* **15**, 13-17 (2020).
- 30 C. Müller, X. Kong, J. M. Cai, K. Melentijević, A. Stacey, M. Markham, D. Twitchen, J. Isoya, S. Pezzagna, J. Meijer, J. F. Du, M. B. Plenio, B. Naydenov, L. P. McGuinness and F. Jelezko. “Nuclear magnetic resonance spectroscopy with single spin sensitivity.” *Nat. Commun.* **5**, 4703 (2014).
- 31 J. Zopes, K. Herb, K. S. Cujia, and C. L. Degen. “Three-Dimensional Nuclear Spin Positioning Using Coherent Radio-Frequency Control.” *Phys. Rev. Lett.* **121**, 170801 (2018).
- 32 M. H. Abobeih, J. Randall, C. E. Bradley, H. P. Bartling, M. A. Bakker, M. J. Degen, M. Markham, D. J. Twitchen and T. H. Taminiau. “Atomic-scale imaging of a 27-nuclear-spin cluster using a quantum sensor.” *Nature* **576**, 411-415 (2019).
- 33 Z. Yang, X. Kong, Z. Li, K. Yang, P. Yu, P. Wang, Y. Wang, X. Qin, X. Rong, C. K. Duan, F. Shi and J. Du. “Structural Analysis of Nuclear Spin Clusters via 2D Nanoscale Nuclear Magnetic Resonance Spectroscopy.” *Adv. Quantum Technol.* **3**, 1900136 (2020).
- 34 N.Y. Yao, L. Jiang, A.V. Gorshkov, P.C. Maurer, G. Giedke, J.I. Cirac and M.D. Lukin. “Scalable architecture for a room temperature solid-state quantum information processor.” *Nat. Commun.* **3**, 800 (2012).
- 35 M. H. Abobeih, J. Cramer, M. A. Bakker, N. Kalb, M. Markham, D. J. Twitchen and T. H. Taminiau. “One-second coherence for a single electron spin coupled to a multi-qubit nuclear-spin environment.” *Nat. Commun.* **9**, 2552 (2018).

- 36 P. C. Humphreys, N. Kalb, J. P. J. Morits, R. N. Schouten, R. F. L. Vermeulen, D. J. Twitchen, M. Markham and R. Hanson. “Deterministic delivery of remote entanglement on a quantum network.” *Nature* **558**, 268-273 (2018).
- 37 C. E. Bradley, J. Randall, M. H. Abobeih, R. C. Berrevoets, M. J. Degen, M. A. Bakker, M. Markham, D. J. Twitchen and T. H. Taminiau. “A Ten-Qubit Solid-State Spin Register with Quantum Memory up to One Minute.” *Phys. Rev. X* **9**, 031045 (2019).
- 38 P. Y. Hou, L. He, F. Wang, X. Z. Huang, W. G. Zhang, X. L. Ouyang, X. Wang, W. Q. Lian, X. Y. Chang, L. M. Duan. “Experimental Hamiltonian Learning of an 11-Qubit Solid-State Quantum Spin Register.” *Chin. Phys. Lett.* **36**, 100303 (2019).
- 39 T. van der Sar, Z. H. Wang, M. S. Blok, H. Bernien, T. H. Taminiau, D. M. Toyli, D. A. Lidar, D. D. Awschalom, R. Hanson and V. V. Dobrovitski. “Decoherence-protected quantum gates for a hybrid solid-state spin register.” *Nature* **484**, 82-86 (2012).
- 40 G. Waldherr, Y. Wang, S. Zaiser, M. Jamali, T. Schulte-Herbrüggen, H. Abe, T. Ohshima, J. Isoya, J. F. Du, P. Neumann and J. Wrachtrup. “Quantum error correction in a solid-state hybrid spin register.” *Nature* **506**, 204-207 (2014).
- 41 J. Cramer, N. Kalb, M. A. Rol, B. Hensen, M. S. Blok, M. Markham, D. J. Twitchen, R. Hanson and T. H. Taminiau. “Repeated quantum error correction on a continuously encoded qubit by real-time feedback.” *Nat. Commun.* **7**, 11526 (2016).
- 42 T. Unden, P. Balasubramanian, D. Louzon, Y. Vinkler, M. B. Plenio, M. Markham, D. Twitchen, A. Stacey, I. Lovchinsky, A. O. Sushkov, M. D. Lukin, A. Retzker, B. Naydenov, L. P. McGuinness and F. Jelezko. “Quantum Metrology Enhanced by Repetitive Quantum Error Correction.” *Phys. Rev. Lett.* **116**, 230502 (2016).
- 43 S. B. van Dam, J. Cramer, T. H. Taminiau and R. Hanson. “Multipartite Entanglement Generation and Contextuality Tests Using Nondestructive Three-Qubit Parity Measurements.” *Phys. Rev. Lett.* **123**, 050401 (2019).
- 44 T. K. Unden, D. Louzon, M. Zwolak, W. H. Zurek, and F. Jelezko. “Revealing the Emergence of Classicality Using Nitrogen-Vacancy Centers.” *Phys. Rev. Lett.* **123**, 140402 (2019).
- 45 N. Kalb, A. A. Reiserer, P. C. Humphreys, J. J. W. Bakermans, S. J. Kamerling, N. H. Nickerson, S. C. Benjamin, D. J. Twitchen, M. Markham and R. Hanson. “Entanglement distillation between solid-state quantum network nodes.” *Science* **356**, 928-932 (2017).
- 46 F. Rozpędek, T. Schiet, L. P. Thinh, D. Elkouss, A. C. Doherty and S. Wehner. “Optimizing practical entanglement distillation.” *Phys. Rev. A* **97**, 062333 (2018).
- 47 N. Zhao, J. Wrachtrup and R. B. Liu. “Dynamical decoupling design for identifying weakly

- coupled nuclear spins in a bath.” *Phys. Rev. A* **90**, 032319 (2014).
- 48 M. D. Hürlimann, S. Utsuzawa, C. Y. Hou. “Spin Dynamics of the Carr-Purcell-Meiboom-Gill Sequence in Time-Dependent Magnetic Fields.” *Phys. Rev. Appl.* **12**, 044061 (2019).
- 49 J. Casanova, Z. Y. Wang, J. F. Haase and M. B. Plenio. “Robust dynamical decoupling sequences for individual-nuclear-spin addressing.” *Phys. Rev. A* **92**, 042304 (2015).
- 50 D. Vilar, M. J. Castro and E. Sanchis. “Multi-label text classification using multinomial models.” *Lect. Notes Artif. Int.* **3230**, 220-230 (2004).
- 51 S. Godbole and S. Sarawagi. “Discriminative methods for multi-labeled classification.” *Lect. Notes Artif. Int.* **3056**, 22-30 (2004).
- 52 M. R. Boutell, J. B. Luo, X. P. Shen and C. M. Brown. “Learning multi-label scene classification.” *Pattern Recognit.* **37**, 1757-1771 (2004).
- 53 G. B. Ou and Y. L. Murphey. “Multi-class pattern classification using neural networks.” *Pattern Recognit.* **40**, 4-18 (2007).
- 54 S. M. Liu and J. H. Chen. “A multi-label classification based approach for sentiment classification.” *Expert Syst. Appl.* **42**, 1083-1093 (2015).
- 55 Y. Lecun, L. Bottou, Y. Bengio and P. Haffner. “Gradient-based learning applied to document recognition.” *P. IEEE* **86**, 2278-2324 (1998).
- 56 K. He, X. Zhang, S. Ren and J. Sun. “Deep Residual Learning for Image Recognition.” Preprint at <https://arxiv.org/abs/1512.03385>. (2015).
- 57 S. Ioffe and C. Szegedy. “Batch Normalization: Accelerating Deep Network Training by Reducing Internal Covariate Shift.” Preprint at <https://arxiv.org/abs/1502.03167>. (2015).
- 58 A. P. Nizovtsev, S. Y. Kilin, A. L. Pushkarchuk, V. A. Pushkarchuk, S. A. Kuten, O. A. Zhikol, S. Schmitt, T. Unden and F. Jelezko. “Non-flipping C-13 spins near an NV center in diamond: hyperfine and spatial characteristics by density functional theory simulation of the C-510[NV]H-252 cluster.” *New J. Phys.* **20**, 023022 (2018).
- 59 P. Vincent, H. Larochelle, I. Lajoie, Y. Bengio and P. A. Manzagol. “Stacked Denoising Autoencoders: Learning Useful Representations in a Deep Network with a Local Denoising Criterion.” *J. Mach. Learn. Res.* **11**, 3371-3408 (2010).
- 60 P. Baldi. in *Proceedings of ICML Workshop on Unsupervised and Transfer Learning* Vol. 27 (eds Guyon Isabelle *et al.*) 37-49 (PMLR, Proceedings of Machine Learning Research, 2012).
- 61 S. Kiranyaz, O. Avci, O. Abdeljaber, T. Ince, M. Gabbouj and D. J. Inman. 1D Convolutional Neural Networks and Applications – A Survey. Preprint at <https://arxiv.org/abs/1905.03554>. (2019).

- 62 Z. H. Wang, G. de Lange, D. Riste, R. Hanson and V. V. Dobrovitski. “Comparison of dynamical decoupling protocols for a nitrogen-vacancy center in diamond.” *Phys. Rev. B* **85**, 155204 (2012).
- 63 H. Oh, J. Yun, M. H. Abobeih, K. Jung, K. Kim, T.H. Taminiiau and Dohun Kim. “Algorithmic decomposition for efficient multiple nuclear spin detection in diamond.” Preprint at <https://arxiv.org/abs/2003.00178>. (2020).
- 64 L. Robledo, L. Childress, H. Bernien, B. Hensen, P. F. A. Alkemade and R. Hanson. “High-fidelity projective read-out of a solid-state spin quantum register.” *Nature* **477**, 574-578 (2011).
- 65 L. Luo, Y. Xiong, Y. Liu and X. Sun. “Adaptive Gradient Methods with Dynamic Bound of Learning Rate.” Preprint at <https://arxiv.org/abs/1902.09843>. (2019).
- 66 J. Kennedy and R. Eberhart. in *Proceedings of ICNN'95 - International Conference on Neural Networks*. 1942-1948 (1995).

ACKNOWLEDGEMENT

석사 기간은 연구를 진행하기에는 다소 짧은 기간임에도, 교수님의 정성스러운 지도와 선배분들의 아낌없는 조언을 받아 좋은 연구 성과로 이어질 수 있었습니다.

김도현 교수님, 제가 평소에 실수도 잦은 편이고 이론적으로 부족한 부분이 많아 힘드셨지요? 늘 세심한 부분까지 놓치지 않고 지도해주셔서 감사드립니다. 앞으로 박사과정에서는 실험과 이론 모두 부족함이 없도록 더욱 정진할 것을 약속드립니다.

끝으로 지원이와 (김)경훈이에겐 이 지면을 빌어 정말 고마웠다는 말을 전하고 싶습니다. 둘 덕분에 이론적으로, 실험적으로도 힘든 점들이 많았던 연구였음에도 마무리를 지을 수 있었습니다. 정말 고마워. 다음 연구에서는 나도 많이 도움이 될 수 있도록 더 노력할게. 앞으로도 같이 열심히 해보자.

ABSTRACT IN KOREAN (국문 초록)

본 논문은 다이아몬드의 질소-결함 (NV) 결함 센터와 상호 작용하는 개별 핵 스핀의 초미세 상호작용 계수를 구하는 새로운 방법론을 제시한다. 다이아몬드의 다양한 점 결함 중 하나인 NV 센터는 하나의 질소 원자와 다이아몬드 격자의 인접한 공공(vacant lattice)으로 구성된 광학 활성 구조체이며, NV 센터내의 전자의 스핀 상태는 ^{13}C 동위 원소의 핵 스핀과의 초미세 상호 작용에 따라 변한다.

심층 신경망 기반 알고리즘을 이용하여 우리는 이러한 전자의 상태를 분석하여 단일 전자 스핀에 연결된 핵 스핀을 효율적이고 자동으로 분석할 수 있는 방법을 개발하였다. 이 연구에서는 핵스핀 검출 및 제어에 널리 사용되는 CPMG-타입의 동적 디커플링 분광법에 중점을 두었다. 우리의 딥러닝 접근 방식은 지금까지 분석하기 어려웠던 정교한 스펙트럼 데이터를 빠르고 자동으로 핵스핀 검출을 가능하게 하였고, 이는 복잡한 구조를 가진 샘플의 효율적인 이미징과 확장된 스핀 큐비트 레지스터의 특성을 분석할 때 응용될 수 있을 것이다.

주요어: 질소-공극 센터, CPMG(The Carr-Purcell-Meiboom-Gill) signal, 딥러닝, 초미세 상호작용

학번: 2010-20380